TEL AVIV UNIVERSITY
RAYMOND AND BEVERLY SACKLER
FACULTY OF EXACT SCIENCES
SCHOOL OF PHYSICS & ASTRONOMY

אוניברסיטת תל-אביב
הפקולטה למדעים מדוייקים
ע״ש ריימונד ובברלי סאקלר
בית הספר לפיסיקה ואסטרונומיה

Statistical Mechanics of Polymers in the Vicinity of Repulsive Probes

Thesis submitted as part of the requirements for the degree of
Master of Science (M.Sc.) in Physics at Tel Aviv University
School of Physics and Astronomy

by

Roy Bubis

This work was carried out under the supervision of
Professor Yacov Kantor

April 2009

ACKNOWLEDGMENTS

I wish to thank my supervisor, Professor Yacov Kantor, for his insightful advice and his guidance, and especially for his endless patience. I also wish to thank Professor Mehran Kardar for his helpful correspondence. I am grateful to my army commanders, who allowed me to pursue my studies during my military service.

I could not have completed this work without the love and support of my parents. This work is dedicated to them.

Contents

ABSTRACT

We study a lattice model of a polymer attached by one end to an impenetrable probe of either a circular or a parabolic shape. This configuration is similar to that used in single-molecule experiments. Three main properties of the polymer are studied: the separation of the endpoint from the tip of the probe, the response to an applied force and the number of available configurations. The data is obtained by performing Monte Carlo simulation on lattice models in two and three dimensions.

The properties of the polymer depend on the ratio between its size and the length scale of the probe. In order to obtain a functional description of the properties we use scaling considerations. The analytical predictions are given for the properties in the limits of polymers much shorter or much longer than the probe length scale.

The results of the simulation for the two probe geometries mostly match theoretical predictions at both limits, and display a monotonic crossover between these two limits. However, the (normalized) response to a lateral force displays a maximum when the size of the polymer is of the same order as the probe length scale. This maximum is most distinct for a circular probe geometry. In addition, the number of available configurations of a polymer near a parabolic probe displays unexpected behavior when the polymer is much longer than the probe length scale. We attempt to explain this behavior by using two geometric bounds to describe the probe.

The results obtained in this work suggest that probes exert an important influence on polymers attached to them when the applied forces are small, and that theoretical interpretation of the experimental results should account for such factors.

1 Introduction

In this work, we study a lattice model of a polymer attached by one end to an impenetrable probe. One of the reasons for interest in this problem is the similarity to the geometries of single-molecule manipulation methods, which have been used in recent years to measure the properties of a single macromolecule directly (rather than relying on measurements of a bulk sample containing many molecules). In these experiments a macromolecule, such as a polymer, is attached between a force probe and a support base. A force is then applied to the polymer via the probe, and the response is measured.

The following section contains a brief overview of these methods. A thorough review can be found in [1–5].

1.1 Single-Molecule Manipulation Methods

Single-molecule manipulation methods may be classified into two main groups: mechanical transducers, which directly contact the polymer under investigation, and external field manipulators, which act from a distance on a handle attached to the polymer end. Several of the methods are depicted in Fig. 1.

In the *scanning force microscope*, also known as the *atomic force microscope* [6], a polymer is attached by one end to the sharp tip (of the order of nanometers at the sharpest point) of a flexible cantilever. The other end of the polymer is attached to a surface upon a movable piezoelectric stage. As the stage is moved vertically, the force applied by the polymer on the cantilever can be measured by the cantilever's deflection. *Glass microneedles* [7] rely on a similar principle — in this case the polymer is attached to the tip of a long and narrow glass tube with a tapered end (on the order of nanometers at the tip). This microneedle is then moved and the force applied by the polymer on it is measured by the microneedle's deflection.

Optical tweezers [8] use focused laser light in order to manipulate a micron-sized bead which is attached to one end of the polymer studied. The other end of the polymer is attached to an immobile bead or surface. The optical tweezer effect is

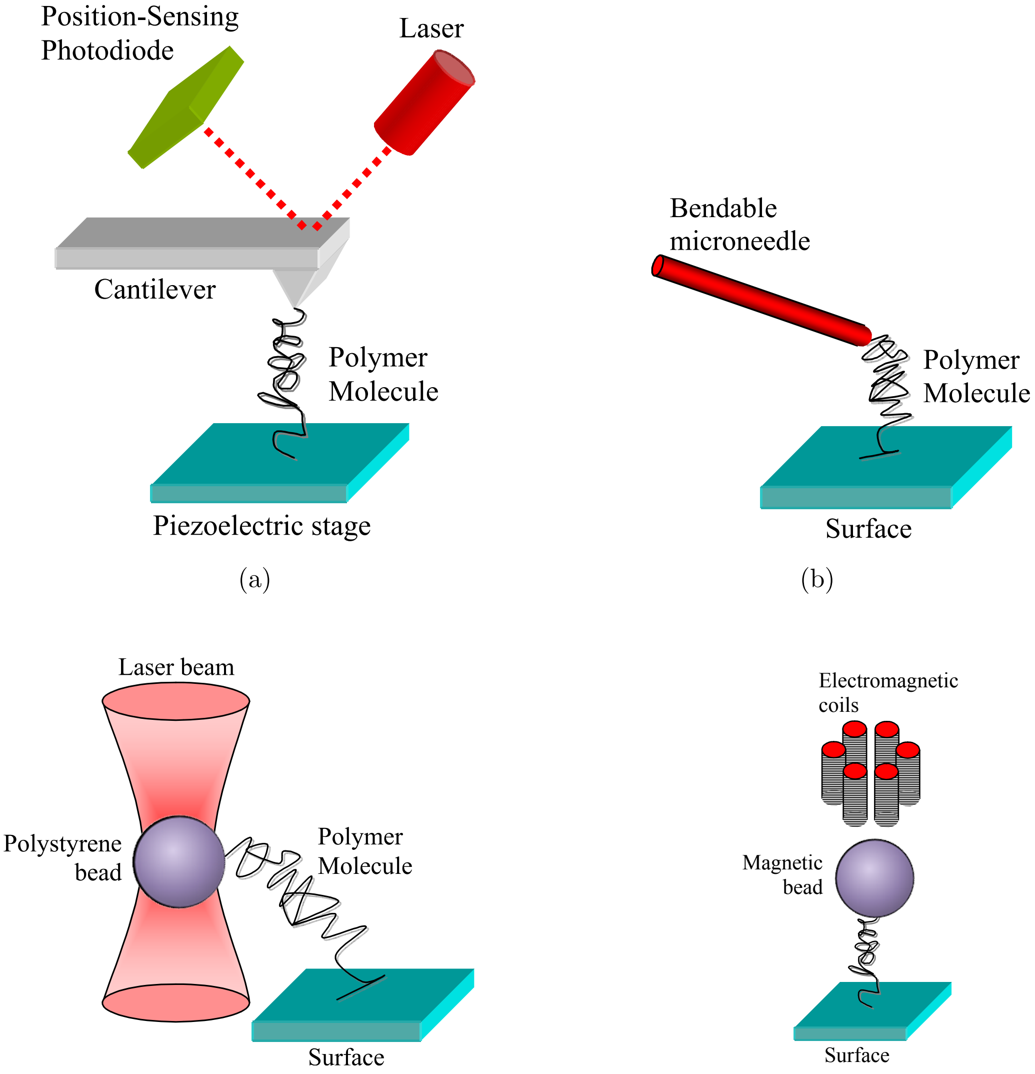

(a) (b)

(c) (d)

Figure 1: Single-molecule manipulation methods: (a) scanning force microscope, (b) glass microneedle, (c) optical tweezers, (d) magnetic tweezers. Based on illustrations in [1, 3–5]

achieved by forces which arise from the intensity gradient of the light produced by the laser — these forces act to center the bead at the focal point of the laser beam. Manipulation of the bead position is possible by changing the focus of the beam. The force applied by the polymer can then be determined by measuring the displacement of the bead from its equilibrium position [4]. *Magnetic tweezers* [9] are similar to optical tweezers, except that the force is applied to a magnetic bead via magnetic fields. This technique can also be used to apply torque (twisting force) to the polymer, in addition to linear force.

In the experiments described above, the applied forces typically range from 0.1pN to 1000pN [1] (the precise range depends on the method used). The application of force stretches the polymers almost to their fully extended length [2], which could be on the order of μm, while in the coiled state, without the application of force, the polymer size is of the order of 10–100 nm.

1.2 Research Question

The methods described in Section 1.1, as well as other single-molecule manipulation methods, share the common characteristic that the polymer is attached to a probe — either a sharp tip or a spherical bead. The purpose of this work is to investigate the effect of such a microscopic probe on the measured properties of the polymer. It must be noted that the geometry considered in this work is of a polymer which is free at one end, whereas in the geometries described above the other end of the polymer is held stationary.

There have been several studies of the properties of polymers attached to a probe that has no length scale. Examples of such probes are a planar wedge in two dimensions [10–13] and a cone in three dimensions [14] — these shapes are completely defined by a single angle. This work focuses on probes which *have* a length scale associated with them: circle or parabola in two dimensions, sphere or paraboloid in three dimensions. We study the dependence of the polymer properties on the ratio between its average size and the length scale of the probe.

We use two different lattice models of polymers, each one applicable in a different regime of polymer solutions (dilute or concentrated solutions). The following properties of the polymer are studied: the separation of the average endpoint position from the tip of the probe, the number of configurations of the polymer and the response of the polymer to an external force applied on it.

1.3 Outline of the Thesis

In Chapter 2, the two polymer models used in this work are described, and the properties of interest are defined. A brief description of the numerical procedures used in this work is also given.

In Chapter 3, we provide the framework of scaling theory, used to describe the dependence of the polymer properties on the ratio of the mean polymer size to the length scale of the probe. We also present the predicted behavior in the limit of polymers much shorter than the length scale of the probe.

Chapters 4 and 5 present the results of polymers near a circle/sphere and a parabola/paraboloid, respectively. In each, we first present the predicted behavior in the limit of polymers much longer than the length scale of the probe. This is followed by the results of numerical simulations and their comparison with theoretical predictions.

The last Chapter presents the main conclusions of the work and discusses future prospects, while Appendix A reviews the numerical procedures used in our work, including a discussion on the efficiency of the algorithms, and Appendix B summarizes numerical results for polymers near a rectangle or cylinder (results which are relevant to Section 5.5).

2 Models for the Study of Polymers

Linear (homo)polymers are long flexible molecules composed of a large number of repeated units, called monomers. The exact properties of such a polymer depend on several factors, such as the type of monomer the polymer is composed of, interactions between the monomers and their number (degree of polymerization). There is also a dependence on external parameters, such as the type of solvent the polymer is dissolved in. Despite this complexity, the *global* properties of polymers can be studied theoretically by omitting most of the details and extracting universal features, which are true for a large class of polymers.

This chapter reviews the two polymer models used in this work: the random walk model and the self-avoiding walk model. These models use great simplifications, replacing continuous space with a discrete lattice and using point objects to model monomers, as well as ignoring the details of the interactions between monomers. Despite these simplifications, the models share certain universal features with real polymers, and these are the features studied here. A polymer in a dilute solution in a good solvent can be modeled by the self-avoiding walk, since the monomers are repelled by other monomers of the same polymer. The situation is different when the polymer is in a concentrated solution consisting of similar polymers. In this case self-interactions are “canceled out” by interactions with other polymers, leading to a behavior resembling a polymer without self-interactions, and fitting the random walk model. A thorough discussion of these models and their applicability to polymer studies can be found in [15,16].

2.1 Definitions

We begin with a review of the properties the models are used to study. The first property is the geometric size of the polymer, which is usually characterized using one of two measures:

1. The *end-to-end vector* $\vec{r}$ is the vector connecting one end of the polymer to the other.

2. The *radius of gyration* r_g is defined as

$$r_\mathrm{g}^2 \equiv \frac{1}{N} \sum_{i=1}^{N} \left\langle (\vec{r}_i - \vec{r}_\mathrm{CM})^2 \right\rangle, \tag{2.1}$$

   where N is the number of monomers, $\vec{r}_i$ the position vectors of the monomers, and $\vec{r}_\mathrm{CM} \equiv \frac{1}{N} \sum_{i=1}^{N} \vec{r}_i$ is the position of the center of mass.

In this work we have chosen to use the end-to-end vector as a measure of the polymer size, since one of the properties of interest is the separation of the endpoint from the probe. In order to define the average geometric size of a polymer, we use the *mean-square end-to-end distance* $R_0^2 \equiv \langle r^2 \rangle$, where the average is taken over all configurations of a polymer of a given length.

The second property studied is the number of configurations $\mathcal{N}_N(\vec{r})$ of a polymer with N monomers, with one point at the origin of coordinates and the other at a point $\vec{r}$. The number of configurations is only finite when studying discrete models, such as the ones used in this work. From this quantity it is possible to calculate the entropy $S(\vec{r})$ associated with all such configurations:[1]

$$S(\vec{r}) = \ln \mathcal{N}_N(\vec{r}). \tag{2.2}$$

In the models used in this work, all configurations have the same energy E, regardless of the end-to-end distance (in the allowed configurations of the models, there is no energy due to interaction between monomers), and therefore the free energy $F(\vec{r})$ of the polymer at a given elongation is only dependent on the entropy:

$$F(\vec{r}) = E - TS(\vec{r}), \tag{2.3}$$

where T is the temperature. Since the kinetic energy in our problem is constant, and we are interested in the static properties of the polymer, we will disregard the kinetic term in our calculations.

The third property studied is the *entropic elasticity*, or *rubber elasticity*[2] [17]. We hold one end of the polymer at the origin and the other end at $\vec{r}$, and calculate the

---

[1] Throughout this work we measure the temperature in units of energy and therefore Boltzmann's constant $k_\mathrm{B} = 1$.

[2] Elasticity which results from the decrease in entropy with the increase in elongation of the polymer.

tension (force) $\vec{f}$ pulling at the ends of the polymer. This can be found from the free energy:

$$\vec{f} = -\vec{\nabla} F(\vec{r}). \tag{2.4}$$

In the equation above we consider the ensemble of all walks with a fixed end-to-end vector, which is analogous to a fixed-volume ensemble. It is also possible to consider an ensemble analogous to a fixed-pressure ensemble: using the ensemble of all walks, we find the elongation due to an external force acting on the ends of the walk (a force $\vec{f}$ at one end and $-\vec{f}$ at the other). In this case we calculate the *average* end-to-end distance $\langle\vec{r}\rangle_{\vec{f}}$ as a result of the force.

In the absence of an external force the probability distribution of the end-to-end vector is $P(\vec{r}) = \frac{\mathcal{N}_N(\vec{r})}{\mathcal{N}_N}$. This distribution is the equivalent of the Boltzmann distribution for this ensemble, since the energy is constant and each configuration has an equal probability. When the force is applied, the probability distribution is shifted by a Boltzmann weighting factor due to the dependence of the energy on the end-to-end vector. Therefore the average end-to-end vector is given by

$$\langle\vec{r}\rangle_{\vec{f}} = \frac{\displaystyle\int \vec{r}\, P(\vec{r}) \exp\left(\frac{\vec{f}\cdot\vec{r}}{T}\right) \mathrm{d}\vec{r}}{\displaystyle\int P(\vec{r}) \exp\left(\frac{\vec{f}\cdot\vec{r}}{T}\right) \mathrm{d}\vec{r}} . \tag{2.5}$$

For a small force the exponents can be expanded in series to obtain, to first order in $\frac{\vec{f}\cdot\vec{r}}{T}$,

$$\begin{aligned}
\langle\vec{r}\rangle_{\vec{f}} &= \frac{\int \vec{r}\, P(\vec{r}) \left(1 + \frac{\vec{f}\cdot\vec{r}}{T} + \cdots\right) \mathrm{d}\vec{r}}{\int P(\vec{r}) \left(1 + \frac{\vec{f}\cdot\vec{r}}{T} + \cdots\right) \mathrm{d}\vec{r}} \\
&\approx \left[\int \vec{r}\, P(\vec{r}) \left(1 + \frac{\vec{f}\cdot\vec{r}}{T}\right) \mathrm{d}\vec{r}\right] \left[1 - \int P(\vec{r}') \left(\frac{\vec{f}\cdot\vec{r}'}{T}\right) \mathrm{d}\vec{r}'\right] \\
&\approx \langle\vec{r}\rangle_0 + \frac{1}{T}\left[\langle\vec{r}(\vec{f}\cdot\vec{r})\rangle_0 - \langle\vec{r}\rangle_0\langle\vec{f}\cdot\vec{r}\rangle_0\right],
\end{aligned} \tag{2.6}$$

where $\langle\cdots\rangle_0$ denotes averaging in the absence of force ($\vec{f} = 0$). In the last expression, the first term is the equilibrium end-to-end vector, and the second term is the linear response to force. We are interested in the force-induced elongation of $r_\parallel$, the component of the endpoint parallel to the force (in an isotropic system this is the only non-zero elongation). It is

$$\langle \Delta r_\parallel \rangle_f \equiv \langle r_\parallel \rangle_f - \langle r_\parallel \rangle_0 \approx \frac{f}{T}\left(\langle r_\parallel^2 \rangle_0 - \langle r_\parallel \rangle_0^2 \right) \equiv \frac{f}{T}\mathrm{var}(r_\parallel), \tag{2.7}$$

where the variance is also evaluated in the absence of force.

When the force is large ($\frac{fR_0}{T} > 1$) the linear approximation is not applicable, and it is necessary to use the Pincus blob model [18]. When the polymer approaches its fully extended length, the applicable models are the freely jointed chain model [19] and the worm-like chain model [20].

In typical single-molecule experiments, the linear approximation is only valid at forces of the order of 0.1pN, which are close the lower end of the force range in most experiments. Future increase in the sensitivity of the experiments will make the linear regime more accessible.

2.2 The Ideal Polymer

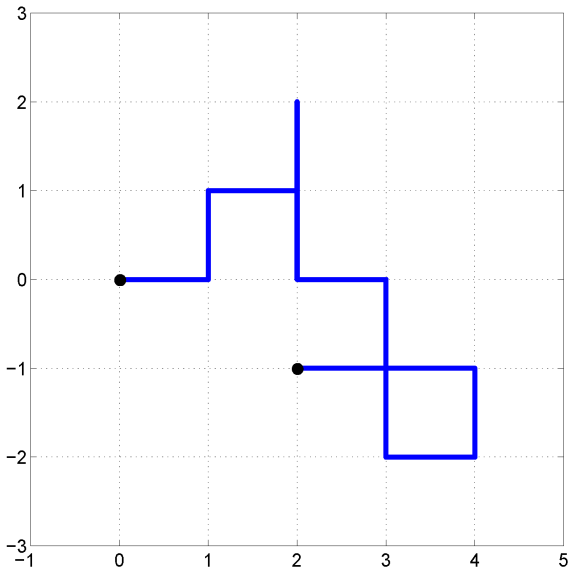

Figure 2: A random walk on the square lattice. The large dots mark the endpoints of the walk. Notice that the walk can cross itself and traverse the same vertices more than once.

Perhaps the simplest realization of a polymer is the lattice random walk (RW) model [21, 22]. This model disregards any interactions between monomers, and replaces continuous space with a discrete lattice. In the model, a polymer of $N + 1$ monomers is replaced by a succession of N steps, each chosen at random, with equal probability, from among the nearest-neighbor sites on a periodic lattice.[3] An example of a random walk for the specific case of the square lattice is seen in Fig. 2. In this work the square and cubic lattices are used for walks in dimensions $d = 2$ and $d = 3$, respectively. We denote a the lattice constant.

At each step the number of possibilities equals the number of neighbors of a lattice site, z, called the *coordination number*. Therefore the total number of configurations $\mathcal{N}_N$ of a walk of length N is:

$$\mathcal{N}_N = z^N. \tag{2.8}$$

The end-to-end vector $\vec{r}$ is the sum of the vectors $\vec{a}_n$, representing the steps of the walk:

$$\vec{r} = \sum_{n=1}^{N} \vec{a}_n. \tag{2.9}$$

Since the different vectors $\vec{a}_n$ are independent of one another, we can draw several conclusions about the end-to-end distance [15]:

1. The mean-square end-to-end distance is linear in N,

   $$R_0^2 \equiv \left\langle r^2 \right\rangle = N a^2. \tag{2.10}$$

   The radius of gyration shows similar behavior.

2. For long walks, the distribution function of the end-to-end vector can be approximated by a Gaussian:[4]

   $$P\left(\vec{r}\right) \approx \left(\frac{d}{2\pi N a^2}\right)^{\frac{d}{2}} \exp\left(-\frac{d\, r^2}{2Na^2}\right). \tag{2.11}$$

---

[3] The usual use of random walks is to describe a particle moving one step per time unit, the variable of interest being its position at time t. We, however, are interested in the line formed by the particle during its walk.

[4] Notice that even for long chains, the use of a continuous Gaussian instead of a discrete distribution causes the distribution to “smear”, eliminating the difference between even and odd coordinates and assigning non-zero probabilities to lengths longer than the fully stretched polymer.

Combining Eqs. (2.8) and (2.11) we obtain the number of RWs of length N, with one end at the origin of coordinates and the other at $\vec{r}$:

$$\mathcal{N}_N(\vec{r}) \approx z^N \left(\frac{d}{2\pi N a^2}\right)^{\frac{d}{2}} \exp\left(-\frac{d\, r^2}{2Na^2}\right). \tag{2.12}$$

From Eqs. (2.2), (2.3) and (2.12), we can find the free energy of a random walk at a given elongation:

$$F\left(\vec{r}\right) = F(0) + \frac{d\,T}{2Na^2} r^2 = F(0) + \frac{1}{2} k r^2, \tag{2.13}$$

giving us the "spring constant" $k \equiv \frac{dT}{Na^2} = \frac{dT}{R_0^2}$ of the ideal polymer. The tension $\vec{f}$, pulling at the ends of a polymer constrained to have an end-to-end vector $\vec{r}$, is $\vec{f} = k\vec{r}$.

All of the properties described above depend on the combination $Na^2 \equiv R_0^2$, rather than a or N separately. That is, if we change the lattice constant from a to $\frac{a}{10}$, and the number of steps from N to $100N$, the same global properties will be observed. This is because these global properties do not depend on microscopic length scales such as the lattice constant, but only macroscopic length scales — in this case the mean size of the walk.

It is also possible to talk of a similar model, but without the constraint of a discrete lattice. In this model, called the *freely-jointed chain* [17], the bonds between successive particles can take any orientation in the d-dimensional space (though they are still of constant length a). Other models introduce "short-range interactions," which govern the relation between successive steps. For example, we can constrain the orientation between successive bonds in the chain. All these models behave similarly to the random walk model. The only difference is the appearance of an effective bond ("persistence") length a_{eff} which replaces a, and an effective number of monomers N_{eff} which replaces N [16].

The simplest non-lattice model of polymer chains is the *Gaussian model*, which assumes that the vector $\vec{a}_n$ connecting successive particles follows a Gaussian distribution

$$p(\vec{a}_n) = \left(\frac{d}{2\pi a^2}\right)^{\frac{3}{2}} \exp\left(-\frac{d\, a_n^2}{2a^2}\right), \tag{2.14}$$

with the mean-square bond length $\langle a_n^2 \rangle = a^2$.

In general, ideal polymer models, that ignore interactions between monomers which are far from each other along the polymer chain, will produce the same global statistical properties for large N. Therefore it is convenient to use models which are as simple as possible, and in this work the lattice model was chosen due to its great simplicity.

2.3 Excluded Volume Effects

The models described in Section 2.2 fail to account for a fundamental physical constraint on the polymer chain — two segments of the polymer cannot occupy the same region in space, no matter how far apart along the polymer they are located. This constraint, called the 'excluded volume effect', is most widely studied in the context of a model called the *self-avoiding walk* (SAW) on a lattice. This model consists of a random walk on a lattice, which is not allowed to intersect itself (Fig. 3).

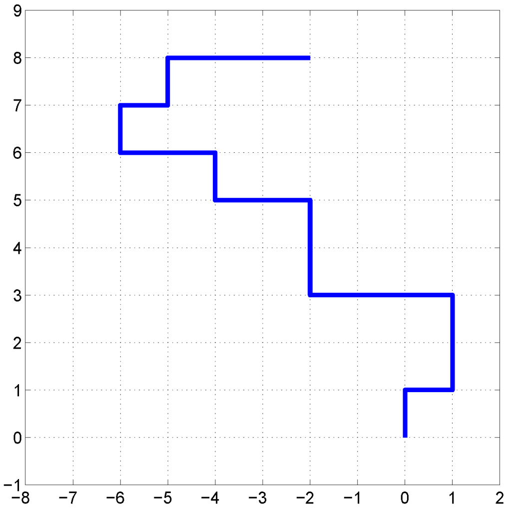

Figure 3: A self-avoiding walk on the square lattice.

Due to the self-avoiding effect, the properties of the chain are altered. The average size of a SAW is larger than that of an unrestricted RW with the same number of steps, and behaves as:[5]

$$R_0^2 \equiv \left\langle r^2 \right\rangle \sim \left\langle r_{\mathrm{g}}^2 \right\rangle \sim a^2 N^{2\nu}, \tag{2.15}$$

with an exponent $\nu = \nu(d)$ which depends on the dimensionality of the lattice: $\nu(2) = \frac{3}{4}$, $\nu(3) \approx 0.5876$ [23–25] (compared to $\nu = \frac{1}{2}$ of the RW model). The exponent ν is a *universal exponent*, i.e. it depends on dimensionality alone and not the lattice details. For $d \geq 4$, this exponent is equal to that of the RW, $\nu(d \geq 4) = \frac{1}{2}$. In this regime, the repulsion between monomers represents only a weak perturbation[6].

The total number of SAWs of length N behaves, for large N, as:

$$\mathcal{N}_N \sim \mu^N N^{\gamma - 1}, \tag{2.16}$$

where μ is an "effective" coordination number, called the *connective constant*, which is somewhat smaller than z, the number of neighbors of a lattice site. For the square lattice, $\mu \approx 2.638$ [26, 27] and for the cubic lattice $\mu \approx 4.684$ [27, 28]. $\gamma = \gamma(d)$ is another universal exponent: $\gamma(2) = \frac{43}{32}$, $\gamma(3) \approx 1.157$ [29,30]. For $d = 2$ this exponent and the exponent ν have been calculated exactly [31].

For a small force f, the linear response of the SAW to force is similar to that of the RW, with a "spring constant" $k \sim \frac{T}{R_0^2}$ (where R_0 is the mean size of the SAW). This result can be derived using the following dimensional argument: The response for a small force is linear in f. The only other dimensional quantities in the system are R_0 and T (the lattice constant a does not appear by itself but only in the combination $aN^\nu \sim R_0$). Therefore, the only possible expression which has the correct dimensionality and is linear in f is

$$\langle \Delta r_{\|} \rangle_f \sim \frac{f R_0^2}{T}.$$

2.4 The Model System

We study a model of a walk attached by one end to an impenetrable surface, with the other end free. The system is athermal, and there are no forces acting between

---

[5] When the notation $\sim$ is used, dimensionless prefactors of order unity are disregarded. The notation $\approx$ is used to signify a numerical approximation or an expansion to a certain order.

[6] The *upper critical dimension* of the SAW model is $d_{\mathrm{c}} = 4$ [21].

the polymer and the surface. Fig. 4 depicts the two geometries considered, for a two-dimensional SAW. The two types of probes are described by the following equations ($d = 2$):

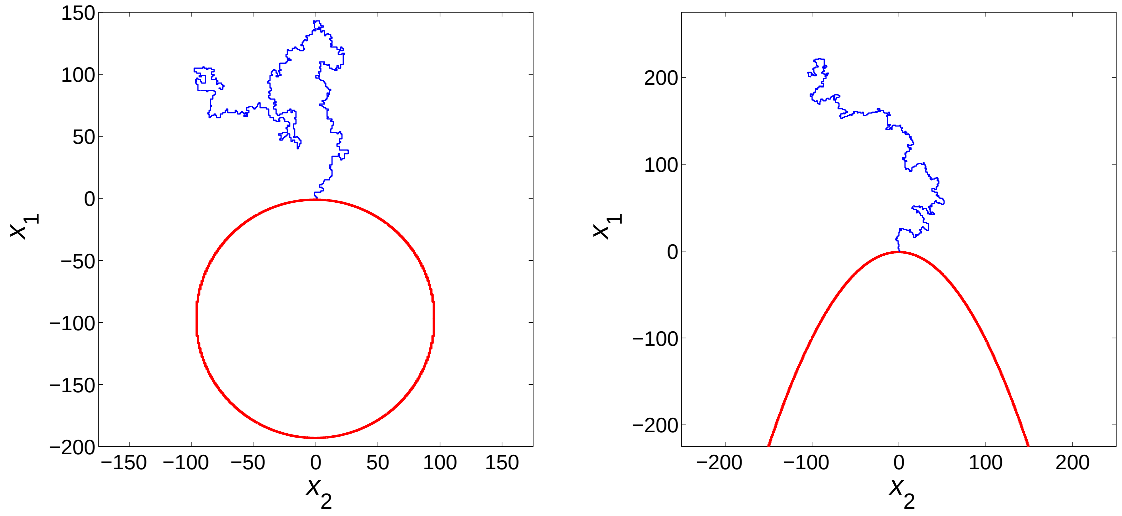

(a) (b)

Figure 4: Self-avoiding walk attached to (a) a circle or (b) a parabola.

$$(x_1 + D + R)^2 + x_2^2 = R^2, \tag{2.17}$$

$$x_1 + Cx_2^2 = -D. \tag{2.18}$$

Eq. (2.17) defines a circle of radius R, and Eq. (2.18) — a parabola with coefficient $(-C)$ (from now on we will use the positive value C when referring to the parabola coefficient). C^{-1} is proportional to the radius of curvature of the parabola at its tip: on smaller scales the parabola appears flat, and on larger scales the curvature of the parabola is expressed. For this reason we will term C^{-1} as the relevant length scale of the parabola, though of course there are other length scales for the parabola, such as its width at a given point.

The first site of the polymer is located at the origin of coordinates, at a distance D from the nearest point of the surface. In order to simplify the problem we set $D = a$, negligible compared to the macroscopic length scales in the model (the mean size of the polymer and the length scale of the probe). At the lower limit of the objects studied in this work, such as a circle of radius $R = 3a$, D is not negligible.

However, at these limits the lattice itself introduces discreteness corrections of order a (the circle in not circular on the lattice). These limits are presented for completeness only. We did not vary D in our simulations to study its effect on the problem.

The impenetrability of the surface means that all points of the walk must be on one side of the curves defined in Eqs. (2.17) and Eq. (2.18), i.e. all points must be outside the probe.

If we draw a line tangent to the probe at the point nearest the initial point of the walk, it will be perpendicular to the x_1 axis and parallel to x_2 (in a generalization to three dimensions, the tangential line is replaced by a tangential plane with two coordinates: x_2 and x_3). For this reason we will usually use $x_\perp$ to denote x_1 and $x_\parallel$ to denote either x_2 or x_3.

2.5 Numerical Methods

In order to study the dependence of the properties of the polymer on its length and on the parameters of the probe, we used numerical methods to simulate random and self-avoiding walks in the presence of an impenetrable surface.

The statistical mechanics of a random walk in the vicinity of a repulsive surface are identical to that of a diffusing particle near an *absorbing* boundary: the paths of diffusers that have not been absorbed by the boundary in the diffusion problem, correspond to permitted configurations in the statistical mechanics problem with a repulsive boundary. In the two-dimensional case we use this analogy: we solve the problem of discrete diffusion of a particle from the origin, where in each time step there is an equal probability for the particle to move to each of the neighboring sites on the lattice. We set the appropriate boundary conditions — probability distribution equal to zero on the surface [22] — and solve the equation numerically to obtain the probability distribution of the particle at time step N. This is the probability distribution of the endpoint of a RW of length N.

In the three-dimensional case the computational resources needed for the method described above become too high, and a different approach is needed. In this case we use Monte Carlo sampling (explained in greater detail below): we create random walks of appropriate length, with no boundary condition. We then calculate the fraction of walks which are “allowed” (i.e. those that do not cross into the surface), and the endpoint distribution of these walks.

The numerical study of the self-avoiding walk model is more elaborate, and therefore we overview the methods used for the SAW in greater detail. Over the years, much of the study of the SAW model has been done using numerical methods, since analytical methods have not yielded satisfactory results for some of the properties of SAWs, especially in three dimensions. Two widely used numerical methods are *exact enumeration* and *Monte Carlo simulation*.

Exact enumeration consists of producing all possible configurations up to a given length, calculating the desired property such as squared end-to-end distance for each configuration, and averaging over the walks. As seen from Eq. (2.16), the number of configurations grows exponentially with N and therefore enumeration is only possible for short chains, and the extrapolation to the limit $N \to \infty$ can introduce a bias which is difficult to estimate.

In a Monte Carlo simulation the configurations are sampled randomly from the equilibrium ensemble distribution, and the average is taken over these configurations only — this makes it possible to explore directly the regime of relatively long SAWs. *Static* Monte Carlo methods generate each configuration independently of previous ones, whereas *dynamic* Monte Carlo methods generate each new configuration by applying a transformation to the previous one. A thorough review of Monte Carlo methods for the self-avoiding walk can be found in [32, 33]. This section contains a brief presentation of the methods used in our simulations.

2.5.1 Dimerization

Dimerization [34,35] is an efficient static Monte Carlo algorithm for generating SAWs. The algorithm utilizes the principle of ‘divide and conquer’, widely used in computer science [36]: In order to produce an N-step walk, we first produce two independent walks of length $N/2$, and try to concatenate them. If the resulting walk is self-avoiding we are done; otherwise, we discard both walks and start again. The process is recursive: the walks of length $N/2$ are produced by concatenating walks of length $N/4$, and so on, until the length of walk needed is short enough to be produced efficiently by a simpler method.

2.5.2 The Pivot Algorithm

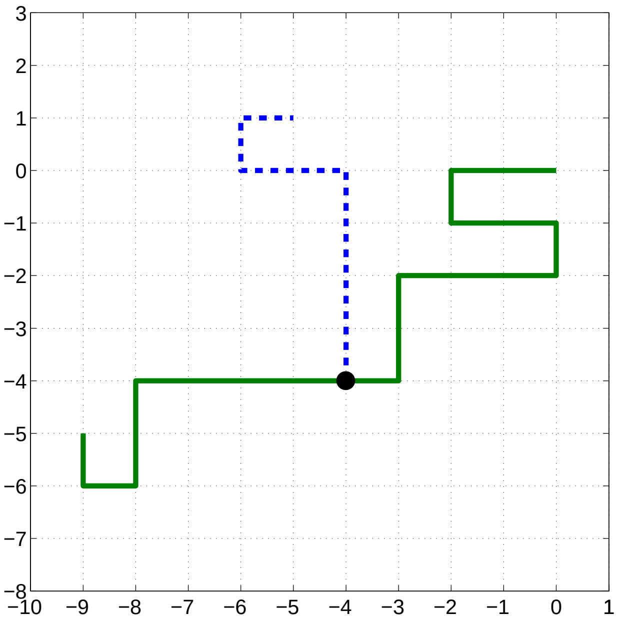

Figure 5: A pivot move on the square lattice. The initial configuration is shown in solid line. A pivot site is selected (denoted by a large dot), and the left part of the walk is rotated 90° clockwise, with the result shown by the dashed line.

While dimerization can be used to produce walks of a few thousands steps, in order to have sufficient statistics we need a large number of samples, and for this reason we use the 'pivot' algorithm [37,38], which is a dynamic Monte Carlo method (i.e. one that generates each new configuration by applying a transformation to the previous one). The algorithm is described schematically in Fig. 5: starting with a given configuration, a random site of the walk is selected as a 'pivot site', which divides the walk into two sections. A random symmetry operation of the lattice is then applied to one of the sections of the walk, with the pivot site as the origin. If the resulting walk is self-avoiding, it is accepted, otherwise the original walk is counted again.

The pivot algorithm is initialized either with a configuration generated using dimerization, or with a straight line configuration. In the second case, the system must first be “thermalized” — an initial run of moves is discarded in order to avoid bias due to the initial configuration. Once the walk is in equilibrium, the relevant observables are calculated after each pivot move, and the mean value is obtained by averaging over all of these configurations.

In order to obtain correct error estimates for the observables, the correlation between the samples must be taken into account. This is done by measuring the autocorrelation time — the number of steps needed for the decay of the autocorrelation function of the observables. For further details of the numerical procedures, the reader is referred to Appendix A.

3 Review of Relevant Results

Before presenting the results of our work, in this chapter we will review some relevant known results in the field. First we overview the properties of polymers near an infinite impenetrable wall, since this geometry corresponds to the limit of polymers much shorter than the length scale of the probe they are attached to (for both circular and parabolic probes). We then overview scaling theory, which is used to derive scaling laws for the dependence of the properties of polymers on the parameters of the system.

3.1 Behavior Near an Impenetrable Wall

When the mean geometric size of the SAW or RW is much smaller than the length scale of the probe, i.e. $\langle r^2 \rangle \ll R^2$ for a circle or $\langle r^2 \rangle \ll \frac{1}{C^2}$ for a parabola, the behavior of the walk is expected to be similar to that of a walk near an infinite impenetrable wall. In this section the relevant properties of such walks are reviewed.

3.1.1 Random Walks

We consider the problem of an ideal polymer with the initial point fixed at the origin of coordinates, in the presence of an impenetrable wall at $x_1 = -D$ (see Fig. 6). This problem is identical to that of a random walker near an absorbing boundary — any walk which has a point on the absorbing boundary is discarded, leaving only walks with all points in the $x_1 > -D$ region. The number of such RWs of length N, starting at the origin of coordinates and ending at point $\vec{r}$, can be calculated using the method of images [22,39]: a negative image is placed at ($x_\perp = -2D$, $x_\parallel = 0$) and the problem is extended to the entire space, leading to the solution

$$\begin{aligned}\mathcal{N}_{N,\text{wall}}(\vec{r}) &= \mathcal{N}_N(\vec{r}) - \mathcal{N}_N(\vec{r} - 2\vec{D}) \\ &\approx z^N \left(\frac{d}{2\pi N a^2}\right)^{\frac{d}{2}} \left\{ \exp\left(-\frac{d\, r^2}{2Na^2}\right) - \exp\left[-\frac{d\,(\vec{r} - 2\vec{D})^2}{2Na^2}\right] \right\}, \qquad (3.1)\end{aligned}$$

where $\mathcal{N}_N(\vec{r})$ was given in Eq. (2.12), and $2\vec{D}$ is the vector connecting the initial point of the walk with the mirror image; in two dimensions, $2\vec{D} = (-2D, 0)$.

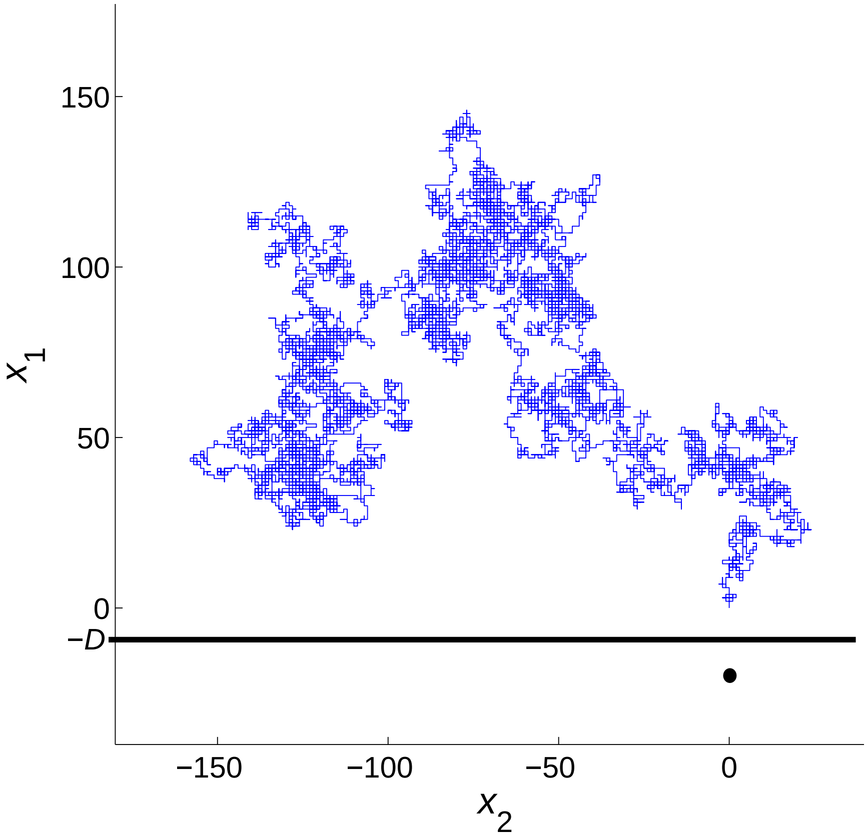

Figure 6: A random walk near an impenetrable wall at $x_1 = -D$, with a mirror image (indicated by a dot) at $x_1 = -2D$.

In order to calculate the total number of walks, we integrate Eq. (3.1) over $-\infty < x_\parallel < \infty$ and $-D < x_\perp < \infty$, to obtain

$$\mathcal{N}_{N,\mathrm{wall}} \approx z^N \mathrm{erf}\left(\frac{D}{a}\sqrt{\frac{d}{2N}}\right) \approx z^N \frac{D}{a}\sqrt{\frac{2d}{\pi N}} = z^N \frac{D}{R_0}\sqrt{\frac{2d}{\pi}}, \tag{3.2}$$

where $\mathrm{erf}(x)$ is the error function, $\mathrm{erf}(x) = \frac{2}{\sqrt{\pi}}\int_0^x e^{-u^2}\,\mathrm{d}u$. In the last approximation we assume that the mean polymer size is much larger than the distance of the wall from the initial point of the walk, $D \ll R_0$, and take the first term in the series expansion of $\mathrm{erf}(x)$ [40].

In order to find the average separation $\langle x'_\perp\rangle_{\mathrm{wall}} \equiv D + \langle x_\perp\rangle$ between the wall and the endpoint, we use the probability distribution of the endpoint in the presence of the wall, $P_{\text{wall}}(\vec{r}) = \frac{\mathcal{N}_{N,\text{wall}}(\vec{r})}{\mathcal{N}_{N,\text{wall}}}$, and calculate

$$\begin{aligned}
\langle x'_\perp \rangle_{\text{wall}} =& D + \int x_\perp \, P_{\text{wall}}(\vec{r}) \, \mathrm{d}\vec{r} \\
=& D + \frac{\sqrt{\frac{d}{2\pi N a^2}}}{\operatorname{erf}\left(\frac{D}{a}\sqrt{\frac{d}{2N}}\right)} \int_{-D}^{\infty} x_\perp \left\{ \exp\left(-\frac{d\, x_\perp^2}{2Na^2}\right) - \exp\left[-\frac{d\,(x_\perp + 2D)^2}{2Na^2}\right] \right\} \mathrm{d}\vec{r} \\
=& D + \frac{D\left(1 - \operatorname{erf}\left(\frac{D}{a\sqrt{\frac{2}{d}N}}\right)\right)}{\operatorname{erf}\left(\frac{D}{a\sqrt{\frac{2}{d}N}}\right)} = \frac{D}{\operatorname{erf}\left(\frac{D}{a\sqrt{\frac{2}{d}N}}\right)} \approx a\sqrt{\frac{\pi N}{2d}} \\
=& R_0 \sqrt{\frac{\pi}{2d}},
\end{aligned} \tag{3.3}$$

where $x_\perp \equiv (\vec{r})_1$ (as defined in Section 2.4), and in the approximation we again assume $D \ll R_0$.

In order to calculate the response to an external force $\vec{f}$ we use Eq. (2.5). Due to the anisotropy of the problem, the elongation depends on the direction of the force. When the force acts in parallel to the wall, $\vec{f} = f\hat{x}_\parallel$ (we shall refer to this as a *lateral* force), the integration over the axis perpendicular to the wall is canceled out and we are left with

$$\langle x_\parallel \rangle_f = \frac{\displaystyle\int_{-\infty}^{\infty} x_\parallel \exp\left(-\frac{d\, x_\parallel^2}{2Na^2} + \frac{f x_\parallel}{T}\right) \mathrm{d}x_\parallel}{\displaystyle\int_{-\infty}^{\infty} \exp\left(-\frac{d\, x_\parallel^2}{2Na^2} + \frac{f x_\parallel}{T}\right) \mathrm{d}x_\parallel} = \frac{Na^2}{dT} f = \frac{f R_0^2}{dT}, \tag{3.4}$$

giving us the spring constant $k = \frac{dT}{R_0^2}$ which is identical to that of the unrestricted ideal polymer, Eq. (2.13).

When the force acts in perpendicular to the wall, $\vec{f} = f\hat{x}_\perp$, the average separation is

$$\begin{aligned}\langle x_\perp\rangle_f =& \frac{\displaystyle\int_{-D}^{\infty} x_\perp \left\{\exp\left(-\frac{d\,x_\perp^2}{2Na^2}\right) - \exp\left[-\frac{d\,(x_\perp+2D)^2}{2Na^2}\right]\right\}\exp\left(\frac{f x_\perp}{T}\right)\,\mathrm{d}x_\perp}{\displaystyle\int_{-D}^{\infty}\left\{\exp\left(-\frac{d\,x_\perp^2}{2Na^2}\right) - \exp\left[-\frac{d\,(x_\perp+2D)^2}{2Na^2}\right]\right\}\exp\left(\frac{f x_\perp}{T}\right)\,\mathrm{d}x_\perp}\\ \approx& \frac{\displaystyle\int_0^\infty x_\perp^2 \exp\left(-\frac{d\,x_\perp^2}{2Na^2}+\frac{f x_\perp}{T}\right)\mathrm{d}x_\perp}{\displaystyle\int_0^\infty x_\perp \exp\left(-\frac{d\,x_\perp^2}{2Na^2}+\frac{f x_\perp}{T}\right)\mathrm{d}x_\perp}\\ =&\sqrt{\frac{Na^2}{2d}}\frac{\sqrt{\pi}e^{w^2}\left[1+\mathrm{erf}(w)\right](1+2w^2)+2w}{1+\sqrt{\pi}we^{w^2}\left[1+\mathrm{erf}(w)\right]},\end{aligned} \tag{3.5}$$

where $D \ll a\sqrt{N}$ is assumed in the approximation, and $w \equiv \frac{fa}{T}\sqrt{\frac{N}{2d}} = \frac{fR_0}{T}\sqrt{\frac{1}{2d}}$.

For small forces ($w \ll 1$), this expression can be expanded in series around $w = 0$, to obtain

$$\langle x_\perp\rangle_f = R_0\sqrt{\frac{\pi}{2d}} + \frac{4-\pi}{2d}\frac{fR_0^2}{T} + \cdots = R_0\left(\sqrt{\frac{\pi}{2d}} + \frac{4-\pi}{2d}\frac{fR_0}{T} + \cdots\right), \tag{3.6}$$

where the constant term is the equilibrium average distance in the absence of force given in Eq. (3.3), and the linear term is proportional to the equilibrium variance of the endpoint position, $\mathrm{var}(x_\perp)$.

When a large force is applied perpendicularly, we expect the polymer to be stretched to such an extent that it is practically unaffected by the wall, and indeed it can be observed from the expression in (3.5) that for $w \gg 1$ we arrive at

$$\langle x_\perp\rangle_f \approx \frac{fR_0^2}{dT},$$

recovering the result of the unconstrained ideal polymer.

3.1.2 Self-Avoiding Walks

The number of SAWs attached by one end to an infinite impenetrable wall is [41]

$$\mathcal{N}_{N,\mathrm{wall}} \sim \mu^N N^{\gamma_1 - 1}, \tag{3.7}$$

where μ is the same connective constant as in Eq. (2.16), and $\gamma_1 = \gamma_1(d)$ is a universal exponent: $\gamma_1(2) = \frac{61}{64}$ (this exact value was found using conformal mapping [12]), $\gamma_1(3) \approx 0.679$ [42–48].

The average separation between the wall and the SAW endpoint behaves as [49]

$$\langle x_\perp \rangle_{\rm wall} \sim a N^\nu \sim R_0, \tag{3.8}$$

which is analogous to the behavior of the RW, Eq. (3.3) (where $\nu = \frac{1}{2}$).

We can expect the linear response to force to also show behavior analogous to the RW model (though no studies have specifically studied this property of the SAW), so that

$$\left\langle \Delta x_{\perp,\parallel} \right\rangle_f \sim \frac{f R_0^2}{T}, \tag{3.9}$$

with a different prefactor for the parallel and the perpendicular response — a smaller prefactor in the perpendicular direction is expected from the analogy to the RW model.

3.2 Scaling Theory

Scaling theory has been successfully used to explain critical phenomena — systems undergoing a phase transition as they approach a critical temperature $\tau_{\rm c}$. The theory has also been applied to polymer systems by drawing an analogy between $\tau - \tau_{\rm c} \to 0$ and $N^{-1} \to 0$ (increasing the chain length is equivalent to approaching the critical temperature) [15].

For a critical system with two degrees of freedom $u \equiv \frac{\tau - \tau_{\rm c}}{\tau_{\rm c}}$ and h (an external field), the following *scaling hypothesis* can be made regarding the singular part[1] of a thermodynamic quantity Q of the system [50–52]:

$$Q(u,h) = u^x \Phi\left(\frac{u}{h^y}\right), \tag{3.10}$$

where Φ is a *scaling function*, and the exponents x, y depend on the critical point being considered. This is equivalent to the assumption that Q is a *generalized homogeneous function* of the variables [53], i.e. there exist two parameters p_1 and p_2 so that

$$Q(\lambda^{p_1} u, \lambda^{p_2} h) = \lambda Q(u,h). \tag{3.11}$$

By setting $\lambda^{p_1} = u^{-1}$, we recover Eq. (3.10), with $x = p_1^{-1}$ and $y = \frac{p_1}{p_2}$

---

[1] The term which diverges at $\tau = \tau_{\rm c}$.

The application of scaling theory to polymer systems consists of two steps [54]. At first we identify the relevant length scales of the system, and use dimensional analysis to write the observables using scaling functions of dimensionless combinations of these variables.

As an example, consider the separation between the endpoint of a polymer and a circular probe. In this problem there are two length scales — the root-mean-squared polymer end-to-end distance R_0 and the radius R of the circle. We assume that no *microscopic* length scales, such as the nearest-neighbor distance a or the distance $D = a$, affect the macroscopic observable sought. Also, the dimensionless quantity N does not appear by itself but only in the combination $aN^\nu \sim R_0$, as was mentioned in Section 2.2. Therefore, an appropriate scaling hypothesis is[2]

$$\langle x_\perp \rangle_{\text{circle}} = R\,\Phi\left(\frac{R_0}{R}\right), \tag{3.12}$$

where $\Phi(s)$ is the scaling function, and $s \equiv \frac{R_0}{R}$ is the scaling variable. This expression has the correct units of length and the scaling function is a dimensionless function of a dimensionless argument.

The second step consists of using plausible assumptions on the behavior of the observables in certain limits to predict asymptotic power laws and guess the shape of the scaling functions. In the example above, we can deduce the behavior in the limit $s \to 0$: at this limit the behavior is that of a polymer near an impenetrable wall and so, as we saw in Section 3.1, $\langle x_\perp \rangle_{\text{circle}} \sim R_0 \sim aN^\nu$. Therefore, at this limit $\Phi(s) \sim s$.

The scaling function $\Phi(s)$ can be calculated numerically, by performing simulations for different values of N and R and plotting $\frac{\langle x_\perp \rangle_{\text{circle}}}{R}$ against $\frac{aN^\nu}{R}$. The resulting plot should show *data collapse* — the data points from the different simulations should all fall on one continuous curve defining $\Phi(s)$. Results of the application of this method for different observables and different configurations are given in the following chapters of this work.

---

[2] For $D \ll R$ there is no difference between $\langle x_\perp \rangle$ and $\langle x'_\perp \rangle \equiv D + \langle x_\perp \rangle$, therefore only the notation of $\langle x_\perp \rangle$ will be used in the following sections.

4 Polymer Near a Circle — Results

In this chapter we present the simulation results of RWs and SAWs near an impenetrable circle or sphere. When the length of the walk is much larger than the radius of the circle or sphere, we expect the problem to resemble a walk originating near an excluded point. Therefore we begin with a review of results for the excluded point problem.

4.1 Random Walks Near an Excluded Point

The properties of a lattice random walk originating near an excluded ('absorbing') point were studied in [55–58]. In this section the results relevant to this work are summarized.

The average separation between the excluded point and the RW endpoint behaves as [56]:

$$\langle x_\perp \rangle_{\text{point}} \sim \begin{cases} a\ln(N) & \text{if } d = 2, \\ a & \text{if } d \geq 3. \end{cases} \tag{4.1}$$

The reason for the different behavior in $d = 2$ is that for $d \leq 2$ the RW eventually visits every point on the lattice [59] (this is known as *recurrence*), so that if a particular point is excluded, the walks which do not reach this point must show a repulsion from it. For $d > 2$, however, the probability of eventually reaching any point remains less than unity as $N \to \infty$ (known as *transience*), so the exclusion of one point does not lead to a long-range effect [57].

The variance of the endpoint coordinate of the walk behaves as [55]:

$$\operatorname{var}(x_{\perp,\parallel}) \sim \begin{cases} \frac{1}{2}Na^2\left[1 + \frac{1}{\ln(N)}\right] & \text{if } d = 2, \\ \frac{1}{3}Na^2\left(1 + \frac{0.15}{\sqrt{N}}\right) & \text{if } d = 3. \end{cases} \tag{4.2}$$

That is, the variance is isotropic, and in the limit of long walks it is equal to the variance of the free RW.

The behavior of the fraction of allowed walks (walks which originate near an excluded point and do not reach it) can be obtained by studying a similar problem:

a random walk which does not return to its starting point. For this problem, the fraction of allowed walks behaves as [55]

$$\frac{\mathcal{N}_{N,\mathrm{point}}}{\mathcal{N}_N} \sim \begin{cases} \frac{\pi}{\ln(N)} & \text{if } d=2, \\ A+\frac{B}{N} & \text{if } d=3, \end{cases} \tag{4.3}$$

where $A \approx 0.66$ and $B \approx 0.29$. This result demonstrates the recurrence of the RW in $d=2$: the fraction of walks which do not reach the excluded point (in this case the origin of the walk) approaches zero as $N \to \infty$. Similar behavior is expected for the fraction of allowed RWs originating several lattice spacings away from an excluded point: a logarithmic decay to zero in the two-dimensional case, and a convergence to a positive constant for higher dimensions.

4.2 Self-Avoiding Walks Near an Excluded Point

The problem of a self-avoiding walk originating one lattice step away from an excluded point is also known as the *persistence* problem, since it is equivalent to setting the first step of the SAW in a given direction and studying the long-distance effects of this constraint.

The separation of the SAW endpoint from the excluded point shows convergence to a constant in dimension $d \geq 3$ [57]. The behavior in two dimensions has still not been conclusively determined, despite extensive research: several studies have found a that the separation diverges as a power law with a small exponent [60–63], another study indicates a logarithmic divergence [64], whereas a more recent study actually claims convergence to a constant [65]. Due to the difficulty distinguishing between the cases, numerical results have not yet been conclusive enough to confirm either conjecture.

As in the RW case, we expect the variance of the walk endpoint position to be similar to that of a free walk, and therefore the linear response should not differ from that of a free SAW.

The fraction of allowed walks for the persistence problem can be obtained in a straightforward manner: the number of allowed SAWs of length N is equal to the number of SAWs of length $N+1$ with the first step constrained to be in a given direction, and therefore

$$\frac{\mathcal{N}_{N,\mathrm{point}}}{\mathcal{N}_N} = \frac{1}{z}\frac{\mathcal{N}_{N+1}}{\mathcal{N}_N} \approx \frac{\mu}{z}\left(1 + \frac{\gamma - 1}{N}\right), \tag{4.4}$$

where $\mathcal{N}_N$ is given by Eq. (2.16), z is the coordination number of the lattice and μ the connective constant of the SAW on the lattice. Unlike the RW case, Eq. (4.4) demonstrates a convergence to a positive constant in two dimensions as well as higher dimensions. This is an example of the transience of the SAW in two dimensions (the probability of a SAW visiting any given point on the lattice remains less then unity as $N \to \infty$).

4.3 Separation From the Circle

The separation of the endpoint of a walk from an impenetrable circle or sphere of radius R can be written in scaling form as

$$\langle x_\perp \rangle_{\mathrm{circle}} = R\,\Phi\left(\frac{aN^\nu}{R}\right). \tag{4.5}$$

In the limit of short walks, $aN^\nu \ll R$, we expect behavior similar to that of a walk near a wall (the walk does not "sense" the curvature of the circle or sphere). At this limit the separation must be independent of R, requiring that $\Phi(s) \sim s$. Thus Eq. (4.5) reduces to $\langle x_\perp \rangle_{\mathrm{circle}} \sim aN^\nu$, matching the behavior of a walk near a wall, given in Eqs. (3.3) and (3.8).

In the limit of long walks, $aN^\nu \gg R$, we expect behavior similar to that of a walk near an excluded point: Two-dimensional RWs are expected to show a logarithmic divergence with N, $\Phi(s) \sim \ln(s)$. Two-dimensional SAWs might show a logarithmic divergence, a power law divergence or a convergence to a constant. Three-dimensional RWs and SAWs should show a convergence to a constant, $\Phi(s) \sim \mathrm{const}$, leading to $\langle x_\perp \rangle_{\mathrm{circle}} \sim R$.

In order to calculate $\Phi(s)$ numerically, simulations of various walk lengths and sphere or circle radii were performed and the average separation was calculated for each set of parameters. The results for the RW model are given in Fig. 7, which shows

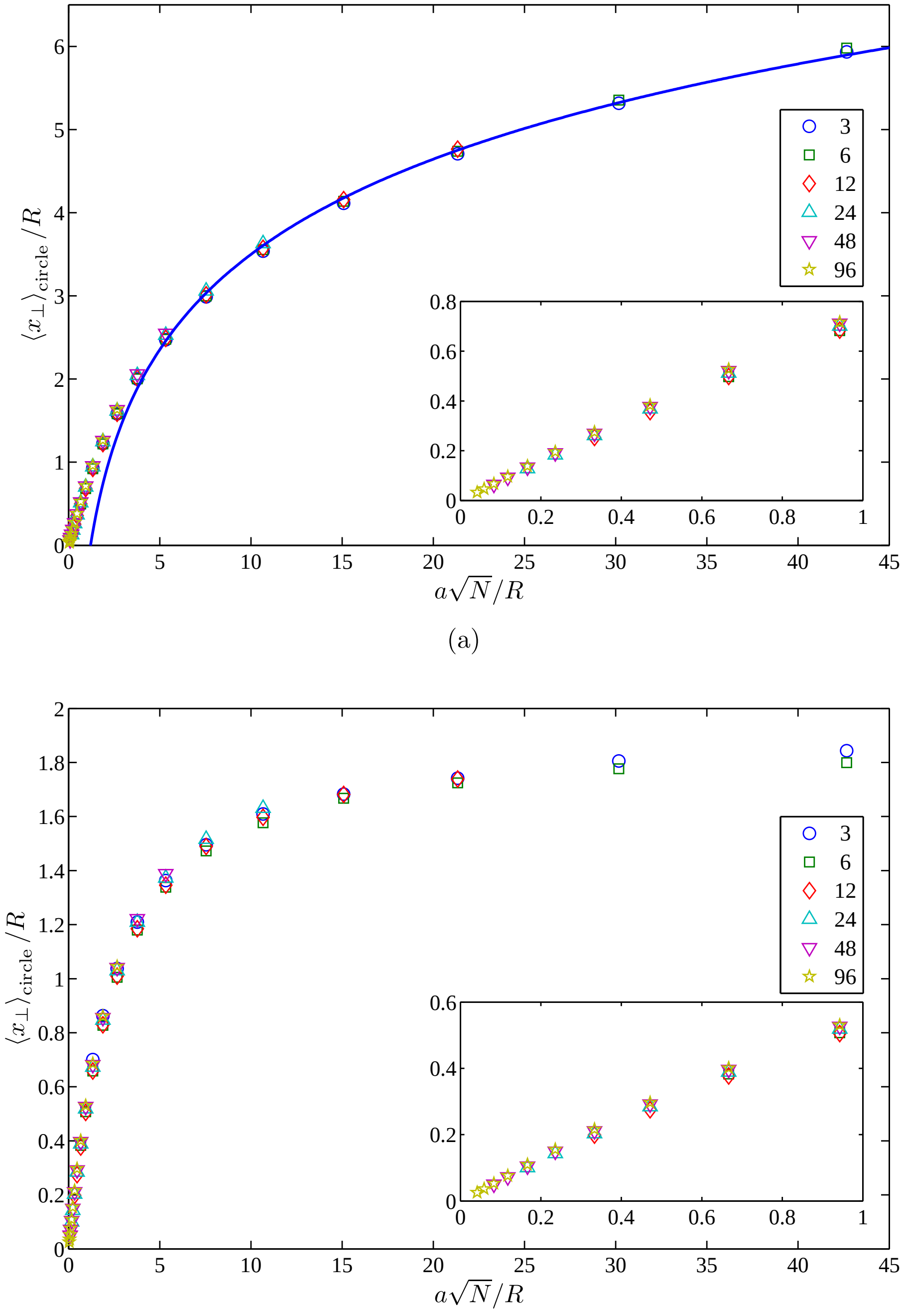

(a)

(b)

Figure 7: Scaling function for the separation of the endpoint of (a) a two-dimensional RW from a circle and (b) a three-dimensional RW from a sphere, for N ranging from 16 to 65536, radii R — from 3 to 96 lattice constants (symbols indicate different radii — see legend), and D equal to one lattice constant. Insets show the behavior for small values of $\frac{a\sqrt{N}}{R}$. In (a), the solid line is a fit to a logarithmic function (see text). Error bars are smaller than the size of the symbols.

$\frac{\langle x_\perp \rangle_{\text{circle}}}{R}$ as a function of $s \equiv \frac{aN^\nu}{R} = \frac{a\sqrt{N}}{R}$ for RWs in two and three dimensions near an excluded circle or sphere, respectively. The plots show excellent data collapse: the points all fall on the same curve, giving us the scaling function $\Phi(s)$.

The insets give the behavior of the scaling function at small values of the scaling variable, $s \leq 1$. At this limit the scaling functions are expected to be linear, with a slope of $\sqrt{\frac{\pi}{2d}}$, matching the the behavior of a RW near a wall, Eq. (3.3). However, the results show a noticeable correction to the linearity of the scaling functions even at low values of s. When a linear fit is performed for $s \leq 1$ the slopes are 0.74 ($d = 2$) and 0.59 ($d = 3$), while a fit for $s \leq 0.2$ gives slopes of 0.81 ($d = 2$) 0.68 ($d = 3$).

In order to account for the nonlinear component of the scaling functions at $s \leq 1$, and to extrapolate the slope at $s = 0$, the data points were fitted to a quadratic function, and the slope of the fit at $s = 0$ was calculated. The results match the predicted values: slopes of 0.84 and 0.71 were obtained in $d = 2$ and $d = 3$, respectively, as compared to the predicted values of 0.89 and 0.72. In addition, the coefficients of the quadratic terms obtained in both fits were much smaller than 1, indicating that the correction to linearity is indeed only a small correction.

The different behavior of long RWs ($s \gg 1$) in different dimensionality can be observed from the graphs. In two dimensions, the scaling function increases logarithmically: Fig. 7a shows a fit to a logarithmic function $\Phi(s) = A\ln(s) + B$ for $5 < s < 60$ ($A = 1.65$, $B = -0.31$). The resulting line fits the simulation results well. The line also fits two data points with $s > 60$, not shown in the graph, though the fit was performed without taking these points into consideration. As expected, the three-dimensional case does not show divergence but tends to a constant, and it was impossible to achieve a good fit to a logarithmic function for these results.

The results for the scaling functions of the SAW model in two and three dimensions are given in Fig. 8. The data for this model also shows excellent data collapse, giving us the appropriate scaling functions. As can be observed from the insets, the behavior of the scaling functions at the lower limit is nearly linear, as in the RW case, though a slight deviation from linearity can be observed for the SAW results as well. In the limit of long walks the separation for the three-dimensional SAW converges to a constant (of about $1.5R$), while the behavior of the two-dimensional SAW at this

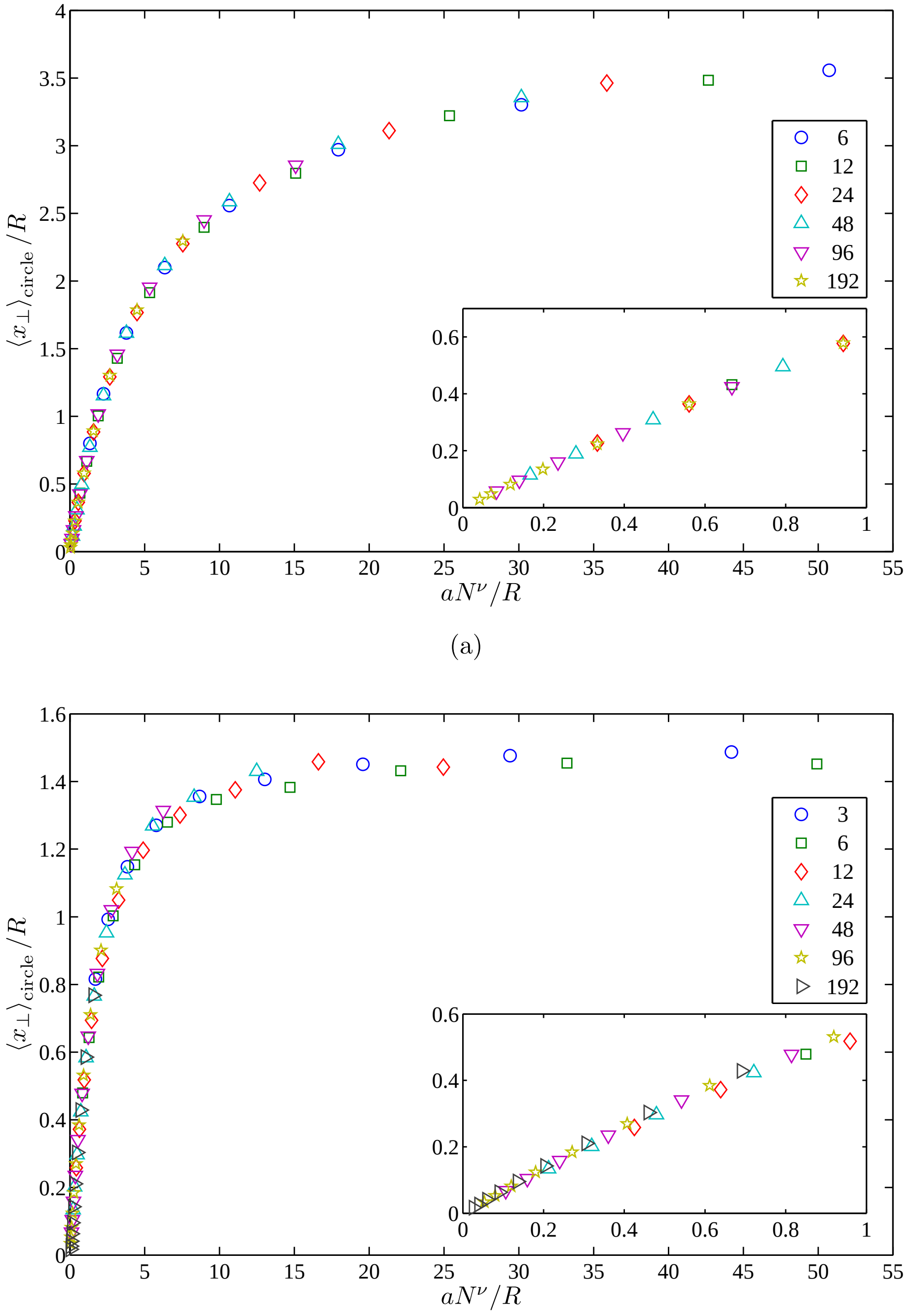

(a)

(b)

Figure 8: Scaling function for the separation of the endpoint of (a) a two-dimensional SAW ($\nu = \frac{3}{4}$) from a circle and (b) a three-dimensional SAW ($\nu \approx 0.5876$) from a sphere, for N ranging from 16 to 16384, radii R — from 3 to 192 lattice constants (symbols indicate different radii — see legend), and D equal to one lattice constant. The insets show the behavior for small values of $\frac{aN^\nu}{R}$. Error bars are smaller than the size of the symbols.

limit is less clear.

In order to determine the behavior of the two-dimensional SAW in the limit of long walks, the results were fitted to a logarithmic function ($A\ln(s)+B$) and to a power law (As^B+G), for $s>5$. The results show that a power law divergence can be ruled out, as the best fit was obtained for a power law approach to a constant ($B<0$). The results of the fit to a logarithmic function were less conclusive: it was possible to perform the fit with reasonable results, but the goodness of the fit was lower than that of the fit for the two-dimensional RW. In addition, the resulting line did not fit data points with larger values of s than those taken into consideration in the calculation of the fit.

In order to further investigate the possibility of a logarithmic divergence for the two-dimensional SAW, plots were made of $\frac{\Phi(s)}{\ln(s)}$ as a function of s^{-1}, and the results for two-dimensional SAWs were compared with those for two-dimensional RWs (Fig. 9). If the scaling function diverges logarithmically, the graph should converge to a positive value as $s^{-1}\rightarrow 0$. For the two-dimensional RW such a convergence can be observed, to a value above 1.5. However, in the two-dimensional SAW there is a clear downward trend as $s^{-1}\rightarrow 0$. This might indicate that the scaling function does not diverge, or that it diverges at a rate slower than logarithmic. However, simulations with larger values of $\frac{aN^\nu}{R}$ are needed for a definite determination. Since the model used in this work was not created to address this question, a clear determination in the matter could not be made.

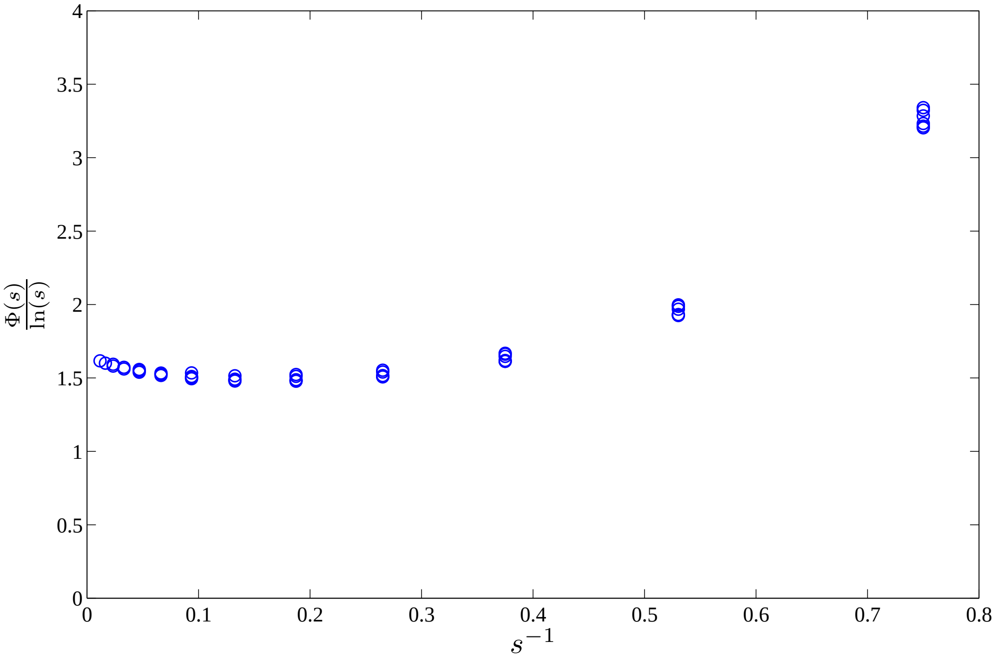

(a)

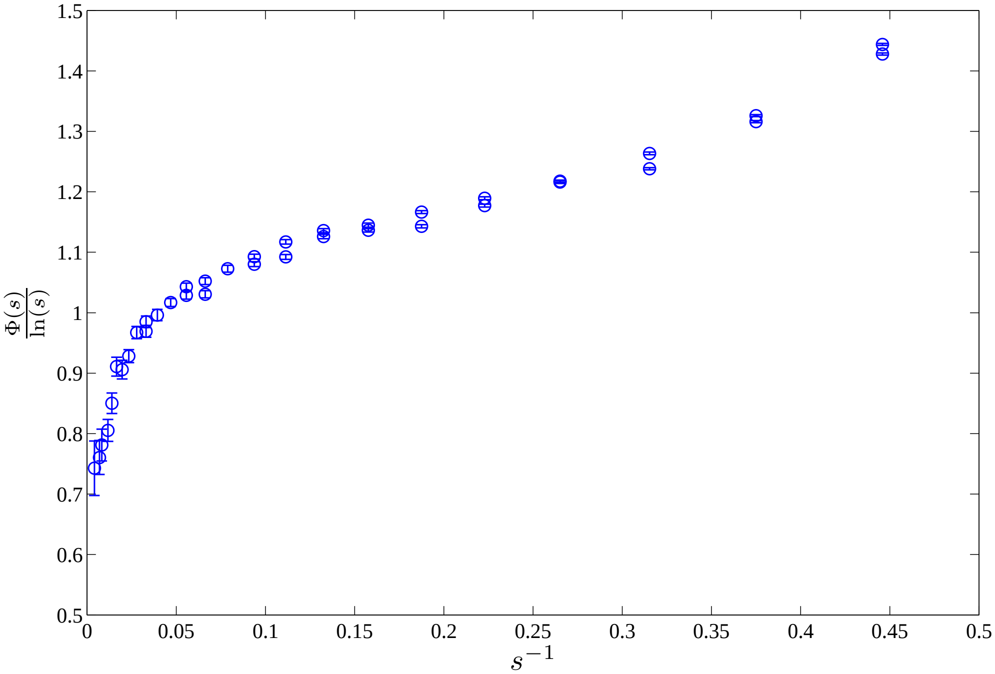

(b)

Figure 9: Plots of $\frac{\Phi(s)}{\ln(s)}$ against s^{-1} for the separation of the endpoint from a circle: (a) two-dimensional RW, (b) two-dimensional SAW. Data points from all the simulation runs are shown as circles, and in (b) error bars are also shown.

4.4 Response to Force

Due to the anisotropy induced by the probe, the response of the polymer to an external force depends on the direction of the force. We define two components: the perpendicular component, for a force acting in direction $x_\perp$, and the lateral component, for a force acting in direction $x_\parallel$. The property studied is the elongation of the polymer in the direction in which the force is applied (though the response is not limited to that direction, since the system is anisotropic).

In Section 2.1, Eq. (2.7), it was shown that the linear response to force is proportional to the variance of the appropriate endpoint component — therefore we will use the variance to express the response to force from now on. The variance can be written in scaling form as:

$$\mathrm{var}(x_{\parallel,\perp}) = a^2 N^{2\nu} \Phi_{\parallel,\perp}\left(\frac{aN^\nu}{R}\right), \tag{4.6}$$

with different scaling functions for the lateral and the perpendicular response.

In the limit of walks much smaller than the circle or sphere we expect behavior similar to that of a walk near a wall: the variance should be proportional to $R_0^2 \sim a^2 N^{2\nu}$, with a smaller proportionality factor for the perpendicular component than the for the lateral one. That is, $\Phi_\parallel(0) > \Phi_\perp(0)$. At the opposite limit, of long walks, the response to force should be isotropic ($\Phi_\parallel(\infty) = \Phi_\perp(\infty)$), since the system is nearly isotropic, with the circle introducing only a small perturbation.

In order to calculate $\Phi_{\parallel,\perp}(s)$ numerically, simulations of various walk lengths and sphere or circle radii were performed and the variance of the appropriate endpoint component was calculated. Fig. 10 shows plots of $\frac{\mathrm{var}(x_{\parallel,\perp})}{a^2 N^{2\nu}}$ as a function of $\frac{aN^\nu}{R}$ for RWs in two and three dimensions, near an excluded circle or sphere, respectively. Again we see good data collapse, as the data points fall on the curves defining the two scaling functions.

We can compare the scaling functions obtained for the RW model with the theoretical results for the two limiting cases. In the limit of short walks we expect behavior similar to that of a walk near a wall: the response to a perpendicular force should match Eq. (3.6), giving $\Phi_\perp(0) = \frac{4-\pi}{2d}$, and the response to a lateral force should match

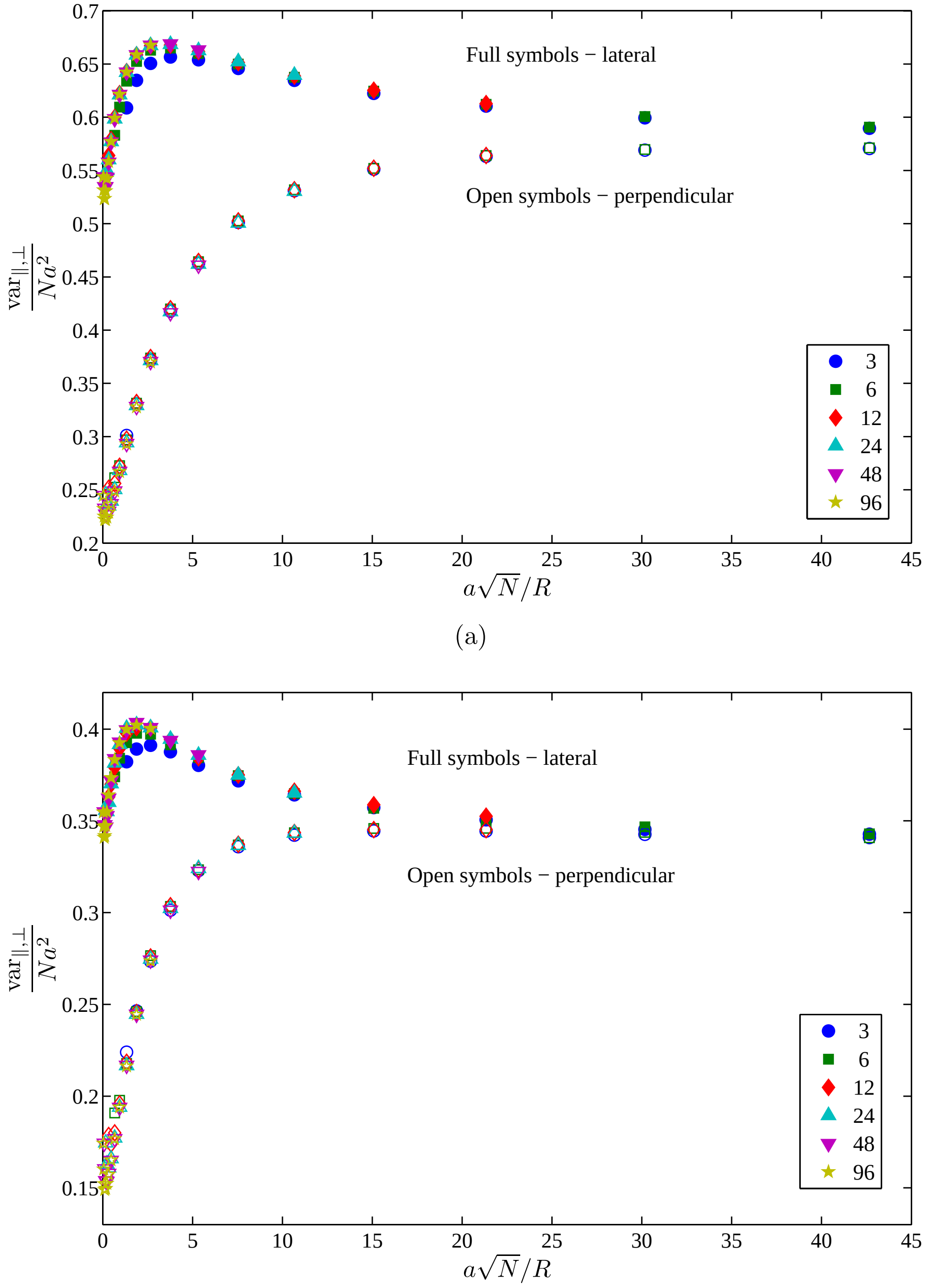

(a)

(b)

Figure 10: Scaling function for the linear response to force of (a) a two-dimensional RW near a circle and (b) a three-dimensional RW near a sphere, for N ranging from 16 to 65536, radii R — from 3 to 96 lattice constants (symbols indicate different radii — see legend), and D equal to one lattice constant. Open (full) symbols indicate response to a perpendicular (lateral) force. Error bars are smaller than the size of the symbols.

Eq. (3.4), giving $\Phi_{\|}(0) = \frac{1}{d}$. The results shown match these predictions very well: for the two-dimensional RW the theoretical prediction is $\Phi_{\perp}(0) \approx 0.215$, $\Phi_{\|}(0) = \frac{1}{2}$ and the numerical results give $\Phi_{\perp}(0) \approx 0.22$, $\Phi_{\|}(0) \approx 0.52$. For the three-dimensional RW the theoretical prediction is $\Phi_{\perp}(0) \approx 0.143$, $\Phi_{\|}(0) = \frac{1}{3}$ and the numerical results give $\Phi_{\perp}(0) \approx 0.15$, $\Phi_{\|}(0) \approx 0.34$.

In the limit of long walks we expect the response to become isotropic, and indeed it can be observed from the figures that the two scaling functions converge as $s \to \infty$. The predicted value for the scaling functions at this limit is $\frac{1}{d}$. In the three-dimensional case the results match this predictions: $\Phi_{\perp,\|}(s) \approx 0.34$ as $s \to \infty$, where the predicted value is $\frac{1}{3}$. In the two-dimensional case, however, the scaling functions appear to converge to a somewhat higher value (0.57 instead of $\frac{1}{2}$). This is due to the slowly decaying logarithmic corrections in two-dimensions, as seen from Eq. (4.2). These corrections are still noticeable at the highest value of the scaling variable shown in Fig. 10b, $s \approx 45$, and we expect the scaling functions to converge to the predicted value for larger values of s. In order to corroborate this claim we performed simulations for longer walks, and were able to observe a downward trend in both scaling functions $\Phi_{\perp}$, $\Phi_{\|}$ for values $s > 45$.

The response to a lateral force exhibits an interesting feature — its scaling function attains a distinct maximum at a value of s between 2 and 4. In order to understand the reason for this behavior it is useful to examine the equilibrium probability distribution of the endpoint of the walk in the presence of the probe. An example is given in Fig. 11, which shows the numerical results for two-dimensional RWs near a circle. It is evident from the figure that the variance of the lateral component of the endpoint increases due to the presence of the probe — the endpoint is repelled to the sides of the probe.

This effect changes as the ratio between the polymer size and the size of the circle changes. The effect is minor when the polymer is much smaller than the probe (Fig. 11a), but becomes more and more pronounced as the polymer length increases in relation to the circle. When the polymer size is of the same order as the circle radius (Fig. 11b), the effect is maximal and a significant portion of the distribution is affected by the circle. As the span of the endpoint distribution overtakes the circle, however,

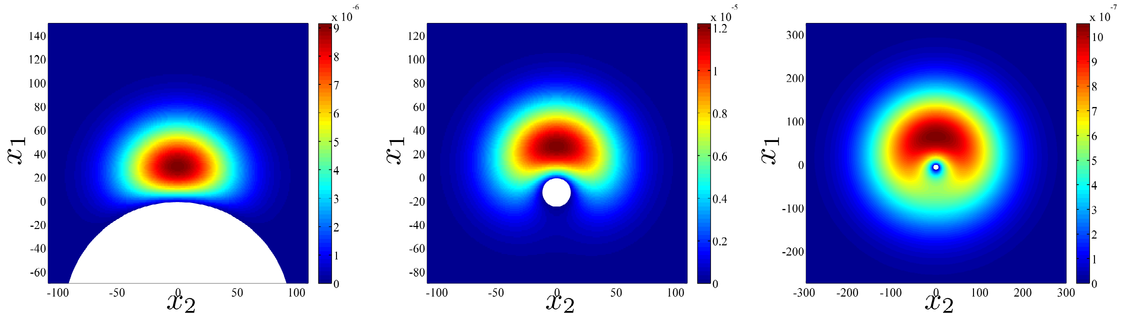

(a) (b) (c)

Figure 11: Probability distribution of the endpoint of a two-dimensional RW near a circle. (a) $N = 2048$, $R = 96a \rightarrow s = 0.5$, (b) $N = 2048$, $R = 12a \rightarrow s = 3.8$, (c) $N = 16384$, $R = 6a \rightarrow s = 21$. The circle in each case is shown in white.

the circle becomes only a small perturbation in the distribution (Fig. 11c), and the effect diminishes. The same effect can also be observed in the three dimensional RW: an example of the probability distribution at the point of maximal variance ($s \approx 4$) is shown in Fig. 12.

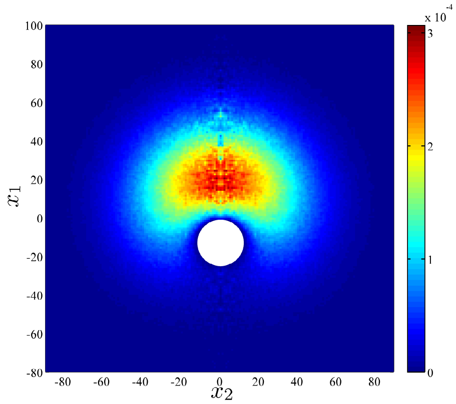

Figure 12: Cross-section at $x_3 = 0$ of the probability distribution of the endpoint of a 2048-step three-dimensional RW, near a sphere of radius $R = 12a$ ($s = 3.8$). The sphere is shown in white.

Fig. 13 shows the results for the SAW model. The data collapse of these results is quite good, though there is a slight separation of the data points for different radii in the graphs depicting the response to a lateral force.

The results for the SAW model mirror those of the RW model. In the lower limit $\Phi_{\parallel}(0) > \Phi_{\perp}(0)$ while in the opposite limit the scaling functions converge, just as

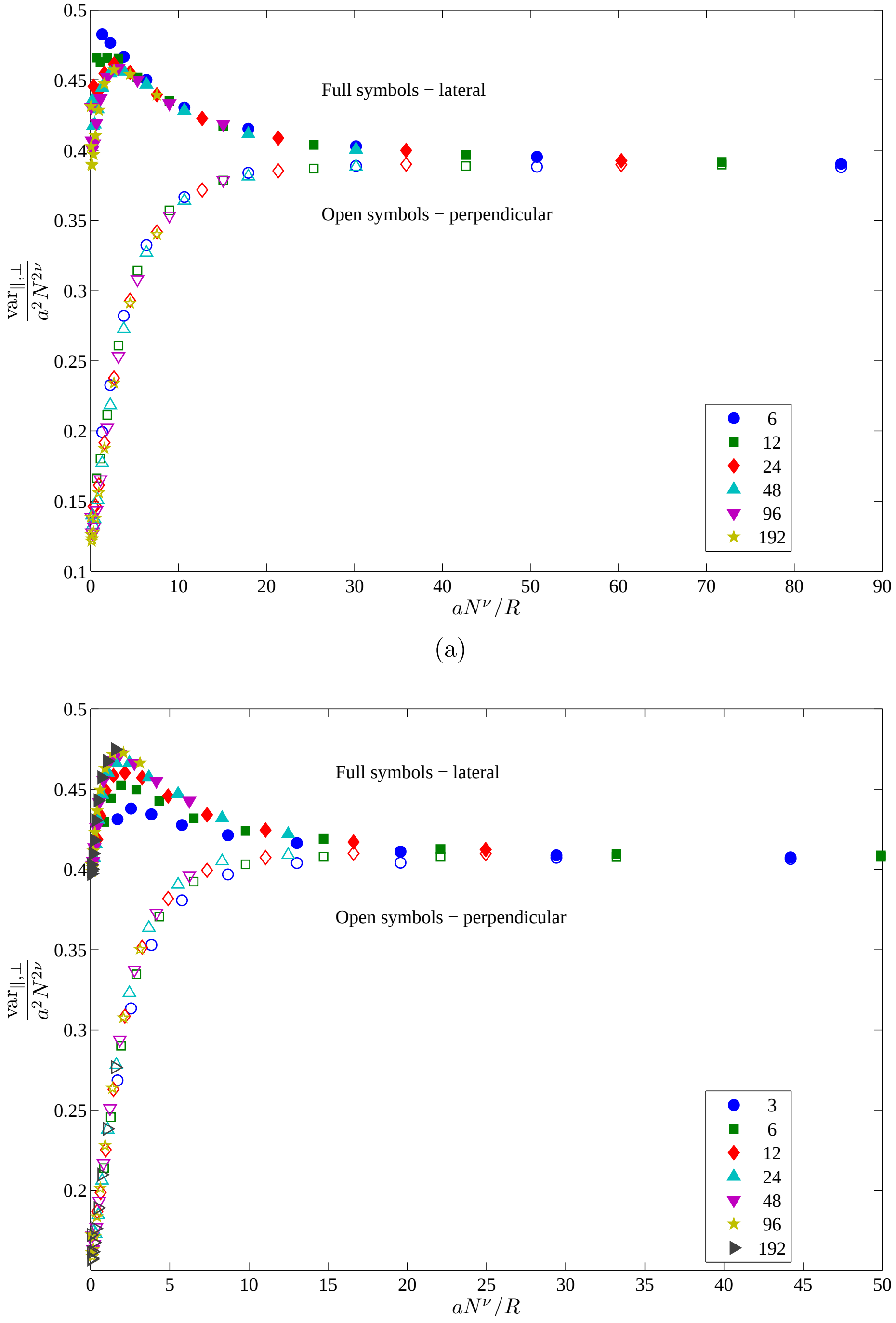

(a)

(b)

Figure 13: Scaling function for the linear response to force of (a) a two-dimensional SAW near a circle and (b) a three-dimensional SAW near a sphere, for N ranging from 16 to 16384, radii R — from 3 to 192 lattice constants (symbols indicate different radii — see legend), and D equal to one lattice constant. Open (full) symbols indicate response to a perpendicular (lateral) force. Error bars are smaller than the size of the symbols.

in the RW case. In addition, the same phenomenon of a maximum in the scaling function for the response to a lateral force can be observed for the SAW results. This maximum in the variance is due to the same reason, as can be seen from Fig. 14, which shows a 512-steps two-dimensional SAW near a circle of radius $24a$ ($s = 4.5$) and a 512-steps three-dimensional SAW near a sphere of radius $12a$ ($s = 3.3$).

Unlike the RW model, when we compare the results of the two-dimensional SAW model with those of the three-dimensional SAW model, we see that $\Phi_{\|,d=2}(0) \approx \Phi_{\|,d=3}(0) \approx 0.4$ and $\Phi_{\perp,d=2}(0) \approx \Phi_{\perp,d=3}(0) \approx 0.15$. This seems counterintuitive, since we expect the relative variance along each axis to decrease with increasing dimensionality: as d increases the width of the distribution in any one axis is smaller, since the fraction of steps taken along that axis is smaller. However, for the SAW model the prefactor in the equation $R_0 \sim aN^{\nu}$ also changes with the dimensionality, and this change compensates exactly for the decrease in relative variance.

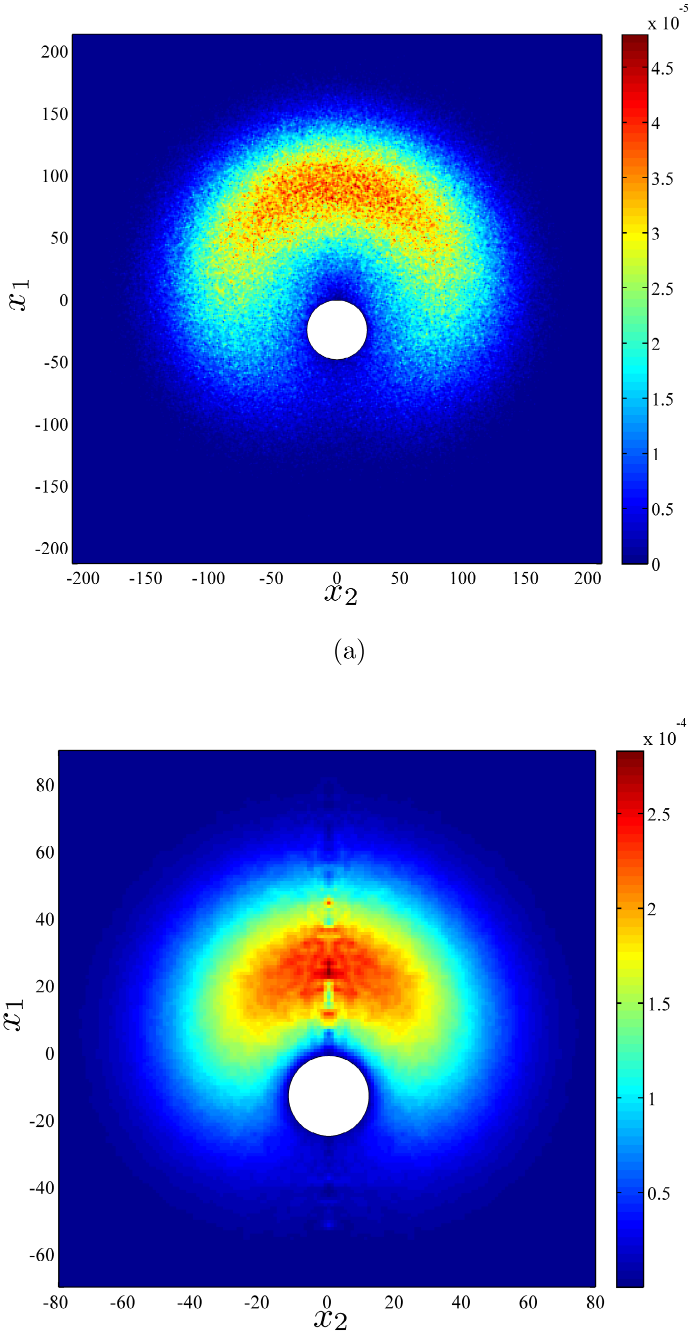

(a)

(b)

Figure 14: Probability distribution of the endpoint of (a) a two-dimensional SAW near a circle of radius $24a$, (b) a three-dimensional SAW near a sphere of radius $12a$ (cross-section at $x_3 = 0$). The circle/sphere is shown in white. In both cases the length of the walk is 512 steps.

4.5 Number of Configurations

This section presents the results for the number of configurations of a polymer near an excluded circle or sphere. In the simulations used in this work, the quantity calculated is $\frac{\mathcal{N}_{N,\text{probe}}}{\mathcal{N}_N}$, the fraction of allowed walks given the constraint of the excluded probe.

We can derive a scaling assumption for this quantity using the following reasoning: When the walk is much shorter than the radius of the circle or sphere, the fraction of allowed walks is similar to that of a walk near an infinite impenetrable wall:

$$\frac{\mathcal{N}_{N,\text{circle}}}{\mathcal{N}_N} \sim N^{\gamma_1-\gamma}, \quad aN^\nu \ll R, \tag{4.7}$$

where γ_1 is the exponent for a walk near a wall: for SAWs the values of γ_1 are given in Section 3.1.2, while for RWs we obtain $\gamma_1 = \frac{1}{2}$ from Eq. (3.2).

On the other hand, when the walk is much longer than the radius of the circle or sphere ($aN^\nu \gg R$), the behavior is expected to match that of a walk near an excluded point. Since the fraction of allowed walks tends to a constant[1] as $N \to \infty$, the fraction of allowed walks near an excluded circle should also tend to a constant, which depends on the radius only. We assume that the crossover between the two behaviors occurs when $R_0 \sim R$ (i.e. when the sizes of the walk and the circle are of the same order).

Inserting the value of N where this crossover occurs into Eq. (4.7) yields the constant $\frac{\mathcal{N}_{N,\text{circle}}}{\mathcal{N}_N} \sim \left(\frac{R}{a}\right)^{\frac{\gamma_1-\gamma}{\nu}}$. Therefore an appropriate scaling assumption is

$$\frac{\mathcal{N}_{N,\text{circle}}}{\mathcal{N}_N} = \left(\frac{R}{a}\right)^{\frac{\gamma_1-\gamma}{\nu}} \Phi\left(\frac{aN^\nu}{R}\right). \tag{4.8}$$

In the limit of short walks we expect $\Phi(s \to 0) \sim s^{\frac{\gamma_1-\gamma}{\nu}}$, eliminating the dependence on R and recovering Eq. (4.7). In the limit of long walks we expect $\Phi(s \to \infty) \to \text{const}$.

In order to calculate $\Phi(s)$ numerically, simulations of various walk lengths and sphere or circle radii were performed, and the fraction of allowed walks was calculated. Fig. 15 shows plots of $\frac{\mathcal{N}_{N,\text{circle}}}{\mathcal{N}_N} \left(\frac{R}{a}\right)^{\frac{\gamma-\gamma_1}{\nu}}$ as a function of $\frac{aN^\nu}{R}$ for RWs in two and three dimensions, near an excluded circle or sphere, respectively.

---

[1] Except for the two-dimensional RW, where the fraction of allowed walks tends to zero.

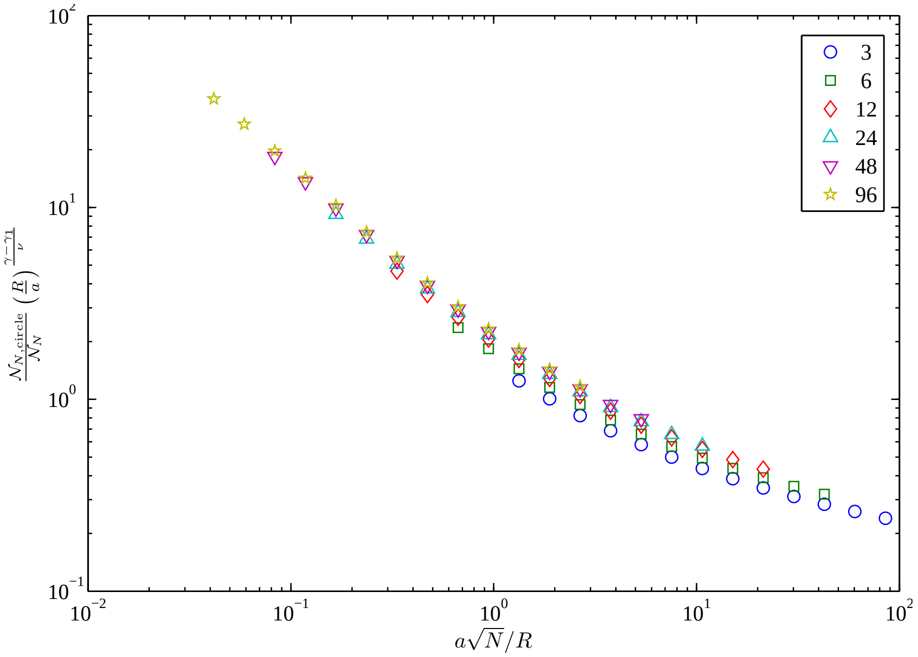

(a)

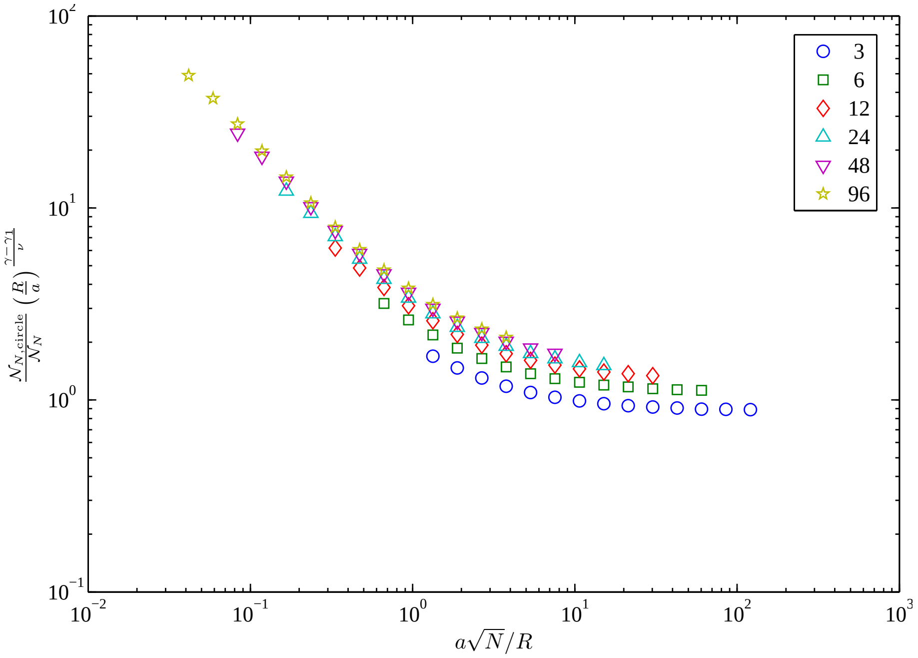

(b)

Figure 15: Scaling function for the fraction of allowed walks for (a) a two-dimensional RW near a circle and (b) a three-dimensional RW near a sphere, for N ranging from 16 to 65536, radii R — from 3 to 96 lattice constants (symbols indicate different radii — see legend), and D equal to one lattice constant.

The data collapse of the results is not quite as good as that obtained in Sections 4.3 and 4.4, as there is a distinct separation of the data points for different radii. This is likely due to the effect of an additional length scale on the observable. There are two additional length scales in the problem: the lattice constant a and the distance D (which we have set equal to a in our simulations). In order to test the possibility that D is the reason for these deviations from scaling, a second set of simulations was performed with D set to zero. The results of these simulations showed similar deviations from scaling, and therefore D can be excluded as the reason for these deviations, and we conclude that the discreteness of the lattice is the likely cause.

In order to account for the effect of the lattice constant, the observable must be written in scaling form as

$$\frac{\mathcal{N}_{N,\text{circle}}}{\mathcal{N}_N} = \left(\frac{R}{a}\right)^{\frac{\gamma_1-\gamma}{\nu}} \tilde{\Phi}\left(\frac{aN^\nu}{R}, \frac{a}{R}\right). \tag{4.9}$$

As the probe size increases in relation to the lattice constant, $\frac{a}{R} \to 0$, this scaling function converges to the one defined in (4.8): $\tilde{\Phi}\left(\frac{aN^\nu}{R}, \frac{a}{R}\right) \to \tilde{\Phi}\left(\frac{aN^\nu}{R}, 0\right) = \Phi\left(\frac{aN^\nu}{R}\right)$. This can be seen from Fig. 15: the data points cluster closer together for larger values of R.

As can be seen from Fig. 15a, the scaling function for the two-dimensional RW actually tends to zero as $s \to \infty$ (due to recurrence), instead of converging to a positive constant, as was our initial assumption when deriving the scaling relation. However, the results still show quite good data collapse in this case, indicating that the scaling relation itself is correct. The scaling function for the three-dimensional RW tends to a positive constant as $s \to \infty$, in accordance with our initial assumption.

In the limit of short walks we expect $\Phi(s \to 0) \sim s^{\frac{\gamma_1-\gamma}{\nu}}$. For the RW model $\frac{\gamma_1-\gamma}{\nu} = -1$, independent of dimensionality. In order to calculate the value of the exponent from the results, a quadratic fit was performed for the graph of $\ln(\Phi)$ as a function of $\ln(s)$, in the region $s \leq 0.4$. The slope of this fit at the data point with lowest value of s gives us the desired exponent. The exponents obtained are -0.98 and -0.95 for the two- and three-dimensional RW, respectively: these exponents agree with the predicted value of $\frac{\gamma_1-\gamma}{\nu} = -1$.

The results for the SAW model are shown in Fig. 16. The data collapse is again

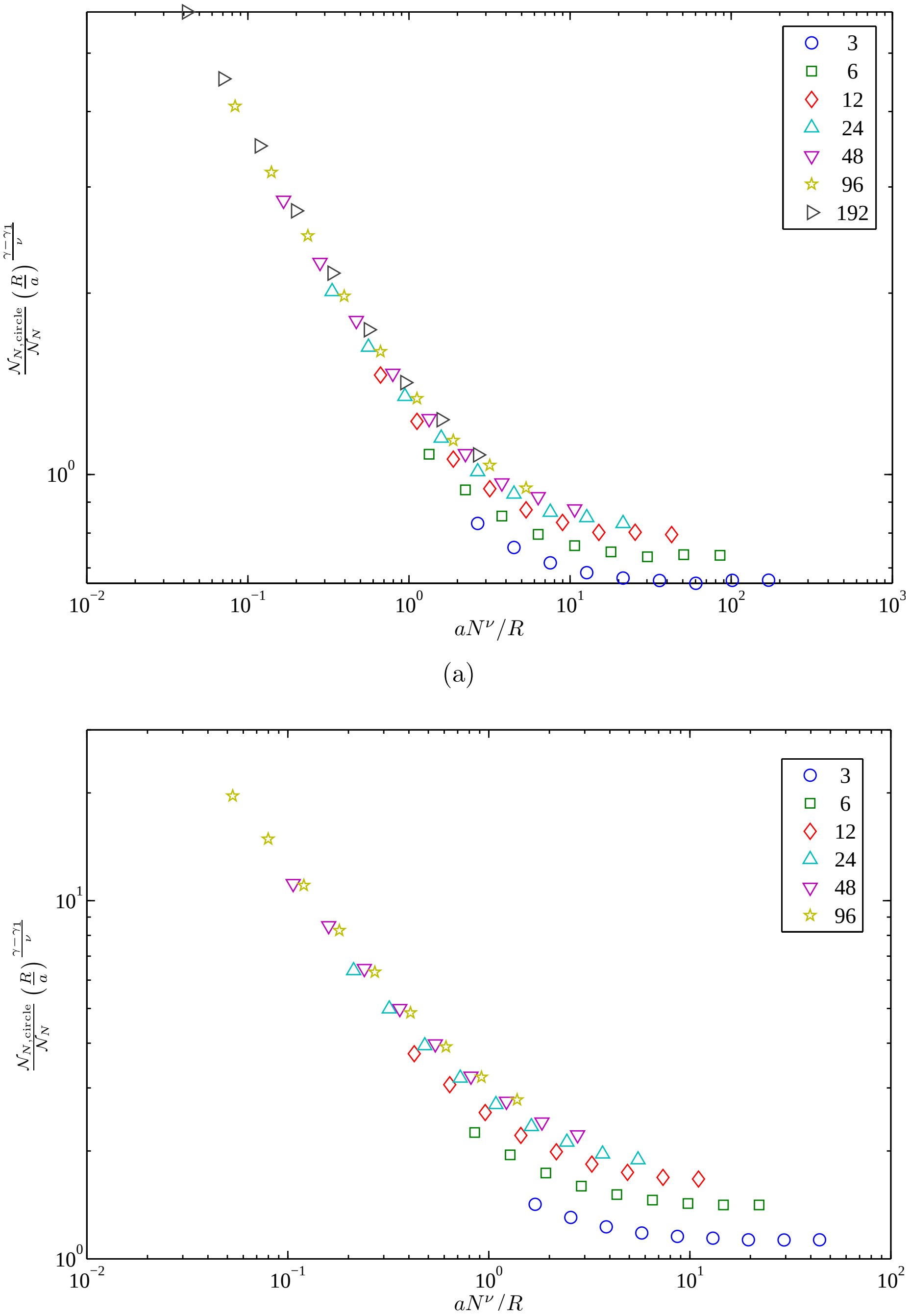

(a)

(b)

Figure 16: Scaling function for the fraction of allowed walks for (a) a two-dimensional SAW near a circle and (b) a three-dimensional SAW near a sphere, for N ranging from 16 to 16384, radii R — from 3 to 192 lattice constants (symbols indicate different radii — see legend), and D equal to one lattice constant.

poorer than for the results of Sections 4.3 and 4.4. The scaling functions of both the two-dimensional and three-dimensional SAW tend to a positive constant as $s \to \infty$. In the limit of short walks we expect $\Phi(s \to 0) \sim s^{\frac{\gamma_1-\gamma}{\nu}}$, where for the two-dimensional SAW $\frac{\gamma_1-\gamma}{\nu} = -\frac{25}{48} \approx -0.52$, and for the three-dimensional SAW $\frac{\gamma_1-\gamma}{\nu} \approx -0.81$. The exponents obtained by the method described above match these predictions quite well: the resulting exponents are -0.53 and -0.78 for the two- and three-dimensional SAW, respectively.

5 Polymer Near a Parabola — Results

This chapter presents the simulation results of RWs and SAWs near an impenetrable parabola or paraboloid. As mentioned in Section 2.4, the length scale which is relevant to our problem is the inverse of the parabola coefficient C, defined in Eq. (2.18). When the length of the walk is much larger than this length scale, we expect the problem to resemble a walk originating near an excluded semi-infinite line ('needle'), extending from $x_1 = -D$ to $x_1 = -\infty$ [66]. Therefore we begin with a review of results for the excluded line problem.

5.1 Random Walks Near an Excluded Line

It is possible to calculate the properties of a RW near an excluded semi-infinite line using the probability distribution of the endpoint of the walk. The distribution can be found by solving the equivalent diffusion problem, with absorbing boundary condition on the half-line $x_\perp < 0$, $x_\parallel = 0$. The exact solutions for two and three dimensions are given in [67], and the asymptotic forms[1] are [57]:

$$P(\rho,\theta,N) \sim \begin{cases} (Na^2)^{-\frac{3}{2}}\rho^{\frac{1}{2}}\exp\left(-\frac{\rho^2}{Na^2}\right)\cos\left(\frac{\theta}{2}\right) & \text{if } d=2, \\ (Na^2)^{-\frac{3}{2}}\exp\left(-\frac{3\rho^2}{2Na^2}\right) & \text{if } d=3. \end{cases} \tag{5.1}$$

The two-dimensional result is given in polar coordinates: $x_1 = \rho\cos(\theta)$, $x_2 = \rho\sin(\theta)$, and the three-dimensional result is given in spherical coordinates: $x_1 = \rho\cos(\theta)$, $x_2 = \rho\sin(\theta)\cos(\phi)$, $x_3 = \rho\sin(\theta)\sin(\phi)$).

The three-dimensional probability distribution is independent of the azimuthal angle ϕ, and *almost* independent of the polar coordinate θ: the dependence on the polar coordinate is expressed only in an infinitesimally small conical region about the excluded line, in which the probability distribution decays to zero. This solution was obtained by taking an absorbing boundary condition of a cone with an opening angle θ_0, and then taking the limit $\theta_0 \to 0$.

Since we use a discrete lattice in our simulations, the minimal lateral distance to the excluded line is one lattice spacing. This means that there is an 'effective'

---

[1] For $a \ll \rho \ll a\sqrt{N}$.

opening angle θ_0 to the line, and this angle vanishes no faster than $N^{-\frac{1}{2}}$ (inversely proportional to the mean length of the walk) [57]. This effective opening angle causes logarithmic corrections to the probability distribution in the three-dimensional case. These corrections are not present in Eq. (5.1), and are a result of the discrete lattice alone.

The average separation between the tip of the excluded line and the RW endpoint can be calculated from the probability distribution given in Eq.(5.1), by performing the integral $\langle x_\perp \rangle_{\text{line}} = \int x_\perp P(\vec{r})\,\mathrm{d}\vec{r}$. In the three-dimensional case the result of this integration is zero, however there are corrections due to the discrete lattice effects. These corrections are given in [57], and in summary the results for the separation are:

$$\langle x_\perp \rangle_{\text{line}} \approx \begin{cases} 0.34aN^{\frac{1}{2}} & \text{if } d = 2, \\ \frac{aN^{\frac{1}{2}}}{\ln(N)} & \text{if } d = 3, \end{cases} \tag{5.2}$$

The variance of the endpoint position in the lateral and perpendicular direction (which is proportional to the linear response to force) can also be calculated from the probability distribution given in Eq. (5.1):

$$\operatorname{var}(x_i) = \langle x_i^2 \rangle - \langle x_i \rangle^2 = \int x_i^2 P(\vec{r})\,\mathrm{d}\vec{r} - \left[\int x_i P(\vec{r})\,\mathrm{d}\vec{r}\right]^2, \tag{5.3}$$

where $x_i = x_\perp,\ x_\parallel$. For $d = 2$ this gives

$$\begin{aligned} \operatorname{var}(x_\perp) &= \left\{ \frac{7}{12} - \left[\frac{\Gamma\left(\frac{7}{4}\right)}{3\Gamma\left(\frac{5}{4}\right)} \right]^2 \right\} Na^2 \approx 0.47Na^2, && (5.4) \\ \operatorname{var}(x_\parallel) &= \frac{2}{3} Na^2, && (5.5) \end{aligned}$$

where $\Gamma(x) \equiv \int_0^\infty t^{x-1} e^{-t}\,\mathrm{d}t$. For $d = 3$ the result of the calculation is identical for the parallel and perpendicular components:

$$\operatorname{var}(x_\perp) = \operatorname{var}(x_\parallel) = \left(\frac{\pi}{6}\right)^{\frac{3}{2}} Na^2 \approx 0.38Na^2. \tag{5.6}$$

However, due to the discrete lattice corrections discussed above, $\langle x_\perp \rangle_{\text{line}} \neq 0$ in three dimensions. This causes corrections of the form $\frac{Na^2}{\ln^2(N)}$ to enter into Eq. (5.6) for $\operatorname{var}(x_\perp)$, since $\operatorname{var}(x_\perp) = \langle x_\perp^2 \rangle - \langle x_\perp \rangle^2$.

The fraction of allowed walks (walks which do not reach the excluded line) is [57]

$$\frac{\mathcal{N}_{N,\mathrm{line}}}{\mathcal{N}_N} \sim \begin{cases} N^{-\frac{1}{4}} & \text{if } d = 2, \\ \frac{1}{\ln(N)} & \text{if } d = 3. \end{cases} \tag{5.7}$$

In the two-dimensional case we see that there is a change in the exponent γ, so that $\gamma_{\mathrm{line}} = \frac{3}{4}$, whereas the result for $d = 3$ shows that there is no change in the exponent γ, but there is a logarithmic correction due to the discrete lattice effect.

5.2 Self-Avoiding Walks Near an Excluded Line

The properties of SAWs near an excluded semi-infinite line were studied in [57,68–71]. The relevant results are summarized in this section.

The average separation between the tip of the excluded line and the SAW endpoint behaves as:

$$\langle x_\perp \rangle_{\mathrm{line}} \sim \begin{cases} aN^{\nu} & \text{if } d = 2, \\ aN^{\sigma} & \text{if } d = 3, \end{cases} \tag{5.8}$$

where σ is a new exponent first reported in [57], which is unique to the geometry of a three-dimensional SAW in the presence of an excluded one-dimensional region. In [69,71] the authors postulate that $\sigma = 1 - \nu \approx 0.41$, while the value obtained from numerical simulations is $\sigma \approx 0.39$.

The linear response to force should show similar behavior to the RW: in $d = 2$ there should be a distinct difference between the lateral and perpendicular response, whereas in $d = 3$ the two components should be equal.

The fraction of walks that do not reach the excluded line behaves as:

$$\frac{\mathcal{N}_{N,\mathrm{line}}}{\mathcal{N}_N} \sim \begin{cases} N^{\gamma_{\mathrm{line}}-\gamma} & \text{if } d = 2, \\ \text{const} & \text{if } d = 3, \end{cases} \tag{5.9}$$

where $\gamma_{\mathrm{line}} = \frac{76}{64}$ [11–13].

For $d = 3$ it is possible to use a geometric argument [71] to show that the fraction of allowed SAWs should tend to a positive constant: The dimension of the generic intersection $A \cap B$ of two geometric sets A and B which are immersed in a space of

d dimensions is

$$d(A \cap B) = d(A) + d(B) - d, \tag{5.10}$$

where $d(S)$ denotes the number of dimensions in which the set S extends to infinity. The Hausdorff dimension [72] of the SAW is $d_{\text{SAW}} = \frac{1}{\nu} \approx 1.7$, and the dimension of the excluded line is $d_{\text{line}} = 1$. Therefore the generic intersection between the two in $d = 3$ is

$$d(\text{SAW} \cap \text{line}) \approx 1.7 + 1 - 3 = -0.3. \tag{5.11}$$

The negative sign of $d(\text{SAW} \cap \text{line})$ means that the two do not generically intersect in dimension $d = 3$ outside any bounded volume (i.e. the fraction of intersections decreases as the bounded volume increases).

5.3 Separation From the Parabola

The separation of the endpoint of a walk from an excluded parabola or paraboloid with coefficient C, can be written in scaling form as

$$\langle x_\perp \rangle_{\text{parabola}} = C^{-1}\, \Phi(aN^\nu C). \tag{5.12}$$

As in the circle geometry, when the walk is much smaller than the parabola length scale, $aN^\nu \ll C^{-1}$, we expect behavior similar to that of a walk near a wall, and therefore $\Phi(s) \sim s$. In the limit of walks much longer than the parabola length scale, $aN^\nu \gg C^{-1}$, we expect behavior similar to that of a walk near an excluded needle (Eqs. (5.2) and (5.8)): Two-dimensional RWs and SAWs are expected to show a power law divergence, $\langle x_\perp \rangle \sim aN^\nu$, leading to $\Phi(s) \sim s$. Three-dimensional RWs should show logarithmic corrections, leading to $\Phi(s) \sim \frac{s}{\ln(s)}$, and three-dimensional SAWs should show a power law divergence with exponent σ, leading to $\Phi(s) \sim s^{\frac{\sigma}{\nu}}$.

The results for the RW model are given in Fig. 17, which shows $C\langle x_\perp \rangle_{\text{parabola}}$ as a function of $s \equiv aN^\nu C$ for RWs in two and three dimensions near an excluded parabola or paraboloid, respectively.

At the lower limit, $s \leq 1$, the scaling functions are expected to resemble those obtained in Section 4.3: the functions are expected to be nearly linear, with a slope

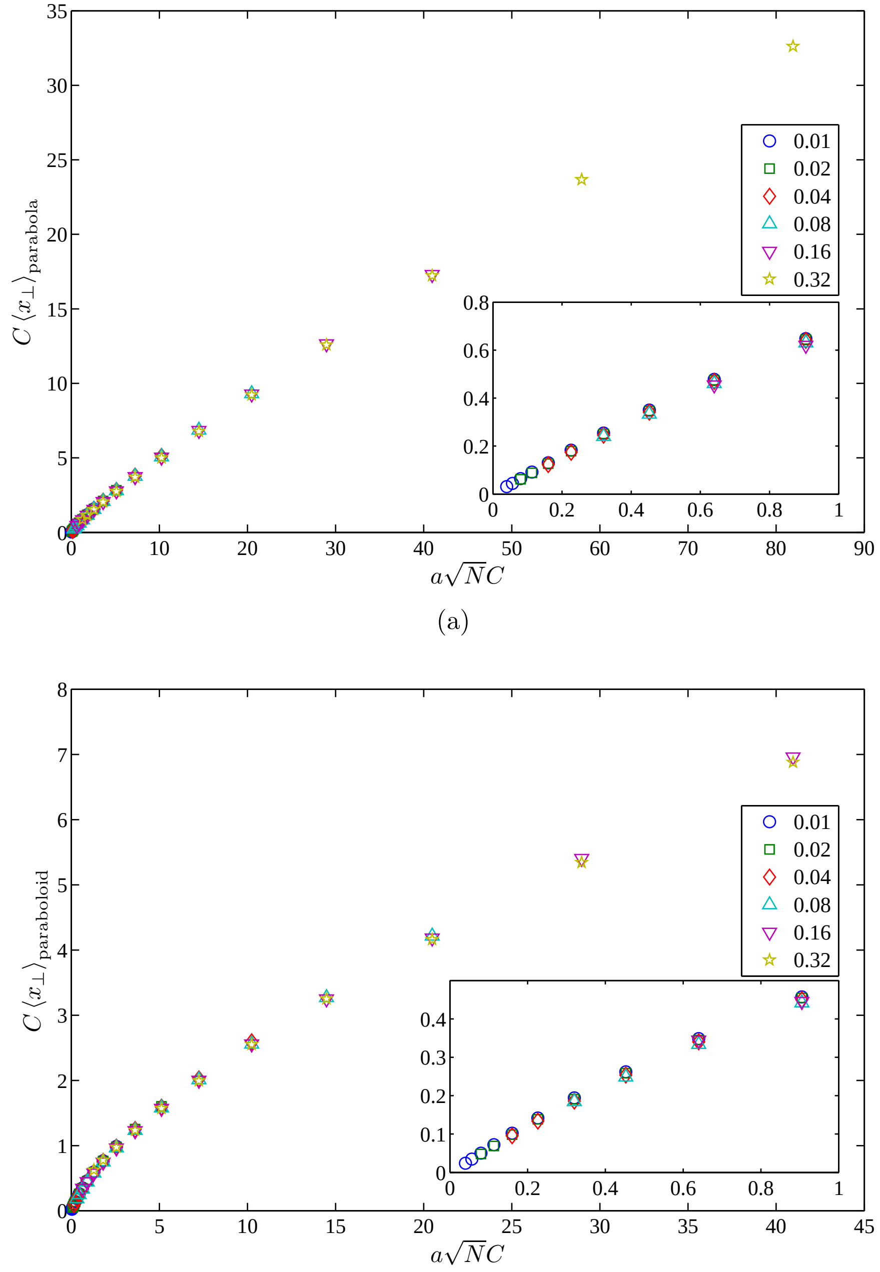

(a)

(b)

Figure 17: Scaling function for the separation of the endpoint of (a) a two-dimensional RW from a parabola and (b) a three-dimensional RW from a paraboloid, for N ranging from 16 to 65536, coefficient C — from $0.01a^{-1}$ to $0.32\ a^{-1}$ (symbols indicate different C — see legend), and D equal to one lattice constant. Insets show the behavior for small values of $a\sqrt{N}C$. Error bars are smaller than the size of the symbols.

of $\sqrt{\frac{\pi}{2d}}$ at $s = 0$. The results fit the predictions quite well: when a quadratic fit is used to extrapolate the slope at $s = 0$, the results are 0.83 for $d = 2$ and 0.66 for $d = 3$, while the predicted values are 0.89 and 0.72, respectively.

In the limit $s \gg 1$, we expect behavior matching Eq. (5.2): linear behavior in two dimensions (with a predicted slope of 0.34), and sublinear behavior ($\frac{s}{\ln(s)}$) in three dimensions. The results match these predictions well: in two-dimensions the slope approaches the predicted value as s increases (a fit for $s \geq 5$ gives a slope of 0.39, while for $s \geq 20$ the slope is 0.38). In three dimensions the behavior of the scaling function matches the predicted sublinear behavior: Fig. 18 demonstrates that $\frac{\Phi(s)\ln(s)}{s}$ tends to a positive constant as $s \to \infty$ (a comparison to the behavior in $d = 2$ is also shown).

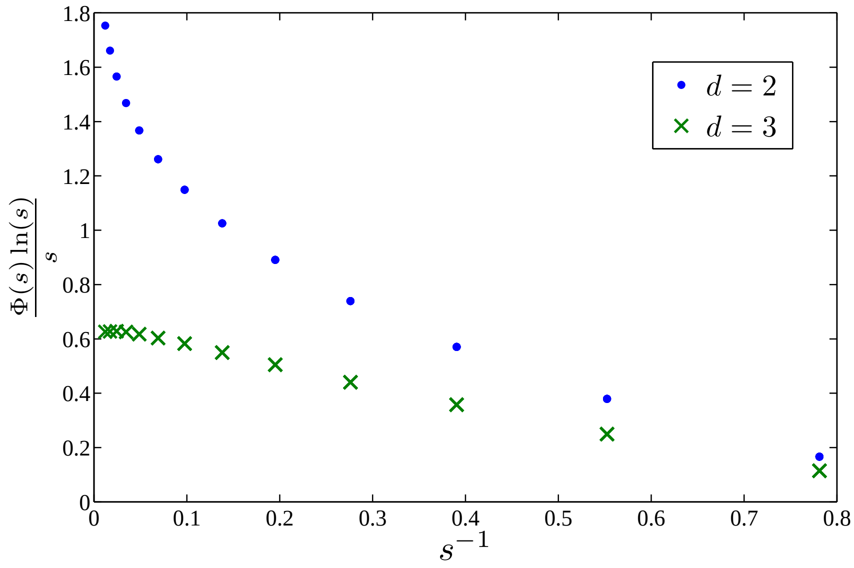

Figure 18: Sublinear behavior in $d = 3$ of the scaling function for the separation of the endpoint of RWs from a paraboloid: when $s^{-1} \to 0$, $\Phi(s)$ is proportional to $\frac{s}{\ln(s)}$. Also shown is the behavior in $d = 2$, where there is no convergence as $s^{-1} \to 0$.

The results for the SAW model are given in Fig. 19. In the limit of short walks the results resemble those obtained for the circle geometry: the scaling functions are linear and of roughly the same slope in both geometries. In the limit of long walks, we expect the two-dimensional scaling function to remain linear (though with a different prefactor than at the lower limit), while the three-dimensional scaling function is expected to behave as $\Phi(s) \sim s^{\frac{\sigma}{\nu}}$ ($\frac{\sigma}{\nu} \approx 0.68$). The results match these predictions quite well: when a power law fit of the form $As^B + D$ is performed for $s > 20$, we obtain for the two-dimensional SAW $B = 0.95$ (where the predicted value is 1) and for the three-dimensional SAW $B = 0.71$ (where the predicted value is 0.68).

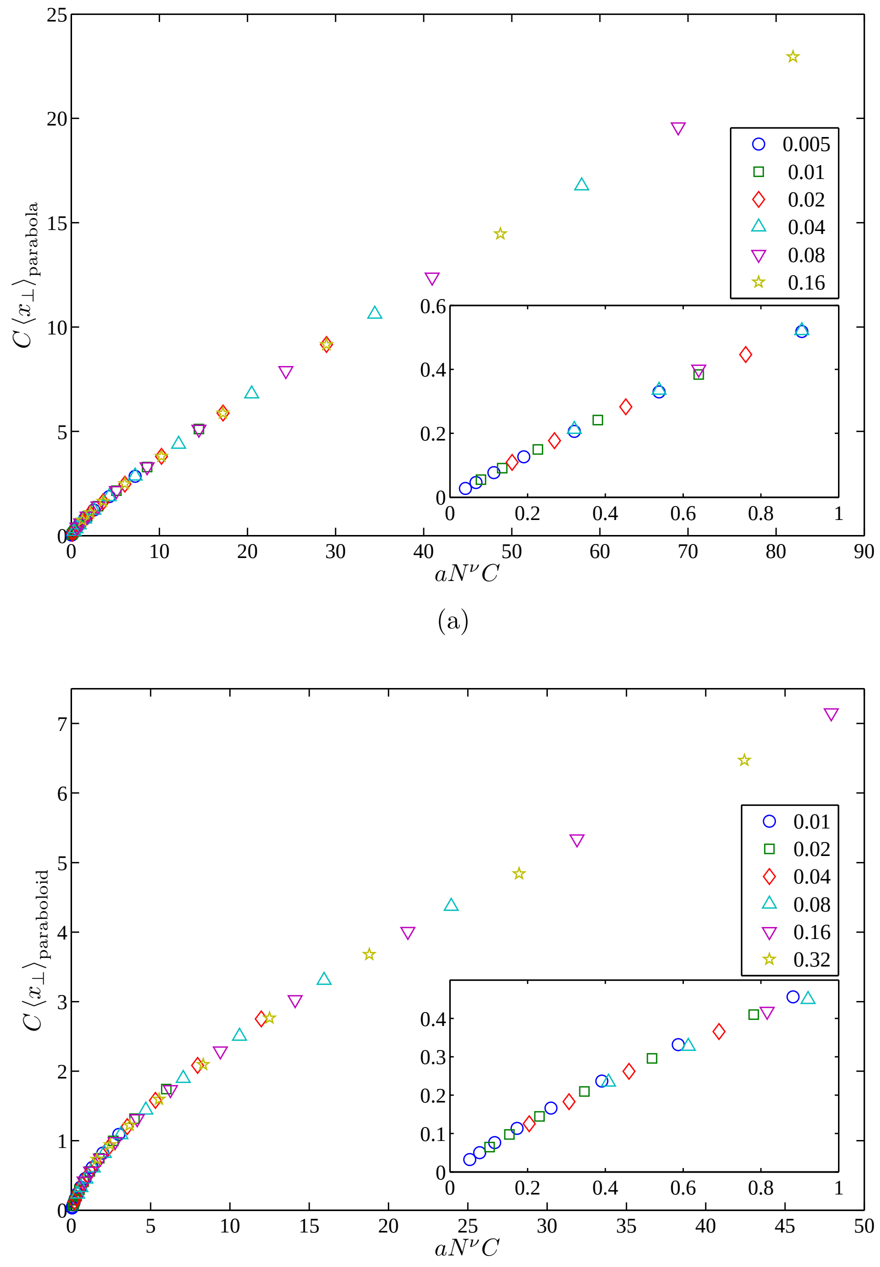

(a)

(b)

Figure 19: Scaling function for the separation of the endpoint of (a) a two-dimensional SAW from a parabola and (b) a three-dimensional SAW from a paraboloid, for N ranging from 16 to 16384, coefficient C — from $0.005a^{-1}$ to $0.32\ a^{-1}$ (symbols indicate different C — see legend), and D equal to one lattice constant. Insets show the behavior for small values of $aN^\nu C$. Error bars are smaller than the size of the symbols.

5.4 Response to Force

Similarly to Section 4.4, the variance of the endpoint position is used in order to find the linear response to force in the lateral and perpendicular directions. The variance can be written in scaling form as:

$$\mathrm{var}(x_{\parallel,\perp}) = a^2 N^{2\nu} \Phi_{\parallel,\perp}\left(aN^{\nu}C\right), \tag{5.13}$$

with different scaling functions for the lateral and perpendicular response.

In the limit of walks much smaller than the parabola length scale we expect behavior similar to that of a walk near a wall. At the opposite limit of long walks, we expect the response to force to remain anisotropic in $d = 2$, but to become isotropic in $d = 3$.

It is possible to compare the results of the RW model, shown in Fig. 20, with the analytical predictions. In the limit of short walks the results resemble those obtained in section 4.3 for walks near a circle: at this limit it is impossible to distinguish between the two types of probes.

In the limit of long walks the results of the RW model in $d = 2$ match the predictions of Eq. (5.5): the predicted perpendicular and lateral variances are $0.47Na^2$ and $\frac{2}{3}Na^2$, respectively, while the numerical results give $0.43Na^2$ for the perpendicular component and $0.68Na^2$ for the lateral component. The results for the RW model in $d = 3$, however, do not match the theoretical predictions quite as well. Theoretically, we expect both the perpendicular and the lateral variance to converge to the value of $0.38Na^2$. The numerical results indicate that the lateral variance converges to a slightly lower value of $0.37Na^2$, while the perpendicular variance seems to converge to an even lower value of $0.31Na^2$.

We saw in Section 5.1 that on a discrete lattice an excluded line actually has an effective opening angle which vanishes as $\frac{1}{N}$, and this effective angle causes correction to the variance which vanish as $\frac{1}{\ln^2(N)}$. In the case of a parabola (in the continuum or on a discrete lattice), there is an effective opening angle which vanishes as $\frac{1}{\sqrt{N}}$, which is expected to cause corrections which decay even slower. This is likely the cause of the discrepancy described above, and we expect that for larger values of s the two scaling functions will converge.

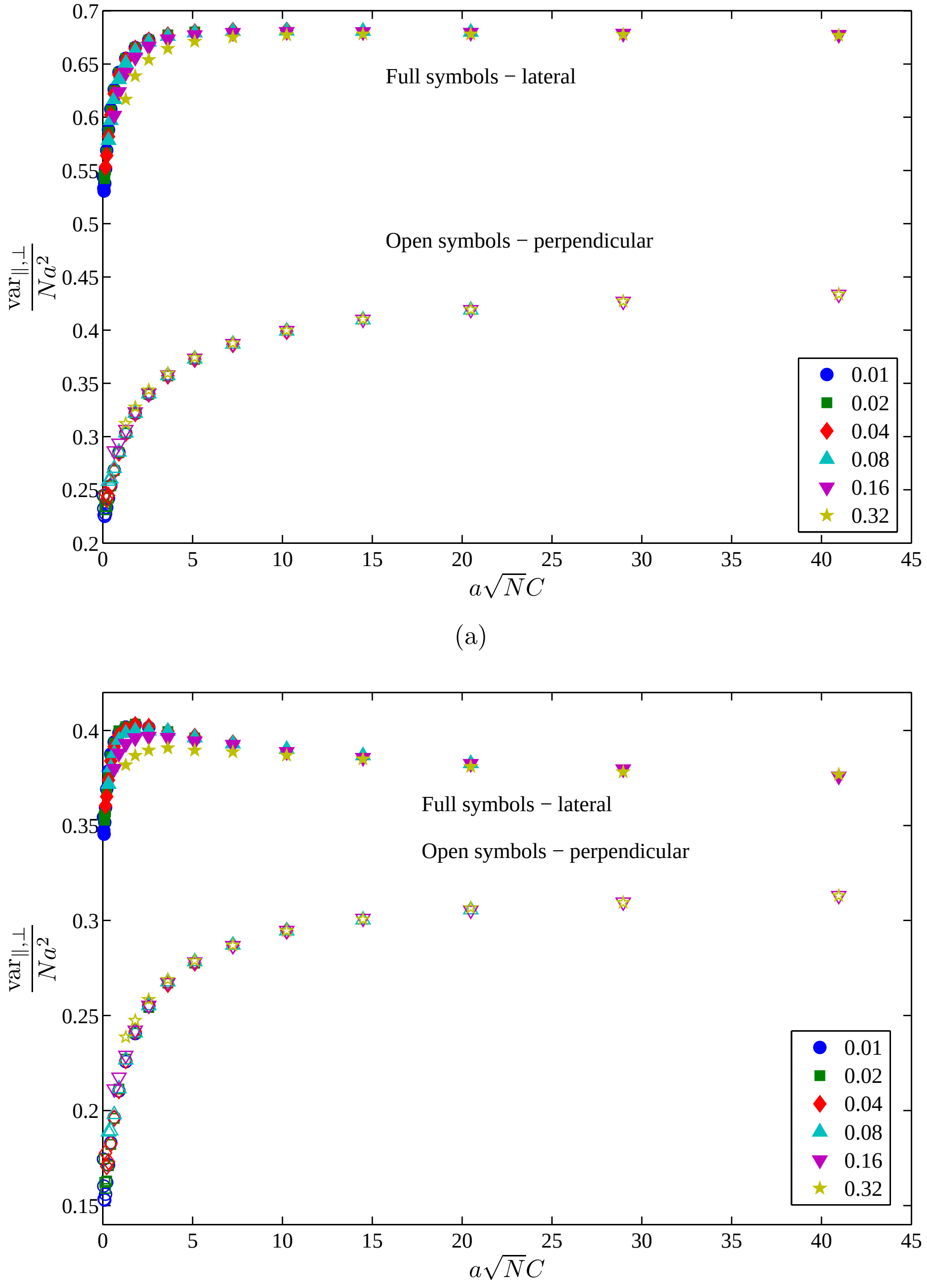

(a)

(b)

Figure 20: Scaling function for the linear response to force of (a) a two-dimensional RW near a parabola and (b) a three-dimensional RW near a paraboloid, for N ranging from 16 to 65536, coefficient C — from $0.01a^{-1}$ to $0.32a^{-1}$ (symbols indicate different C — see legend), and D equal to one lattice constant. Open (full) symbols indicate response to a perpendicular (lateral) force. Error bars are smaller than the size of the symbols.

The three dimensional results show a maximum in the scaling function for the lateral response, for values of s between 2 and 4, similarly to the results for the circle geometry though much less distinctly. This maximum can be explained by the same reasoning as used in Section 4.4.

The results for the SAW model are shown in Fig. 21. The results show quite good data collapse, except for the lateral response to force of the two-dimensional SAW, which shows a noticeable deviation at low values of s. This deviation is an effect of the discrete lattice: when the values of the mean end-to-end distance R_0 and the parabola coefficient C are low, the curvature of the parabola cannot be expressed on the discrete lattice at distances comparable to the mean end-to-end distance of the walk. This effect is also present in other simulation results, though much less noticeably.

Disregarding the deviation due to this discreteness effect, the results for the SAW model at the lower limit $s \ll 1$ match those obtained for SAWs near a circle, as expected. In the limit of long walks the results resemble those obtained for RWs near a parabola. In particular, the three-dimensional results show lateral and perpendicular scaling functions which do not quite converge, just as the RW results. However, as in the RW model, we expect the two functions to converge at larger values of s. The SAW results in three dimensions also exhibit a maximum in the scaling function for the response to a lateral force, as in the RW model.

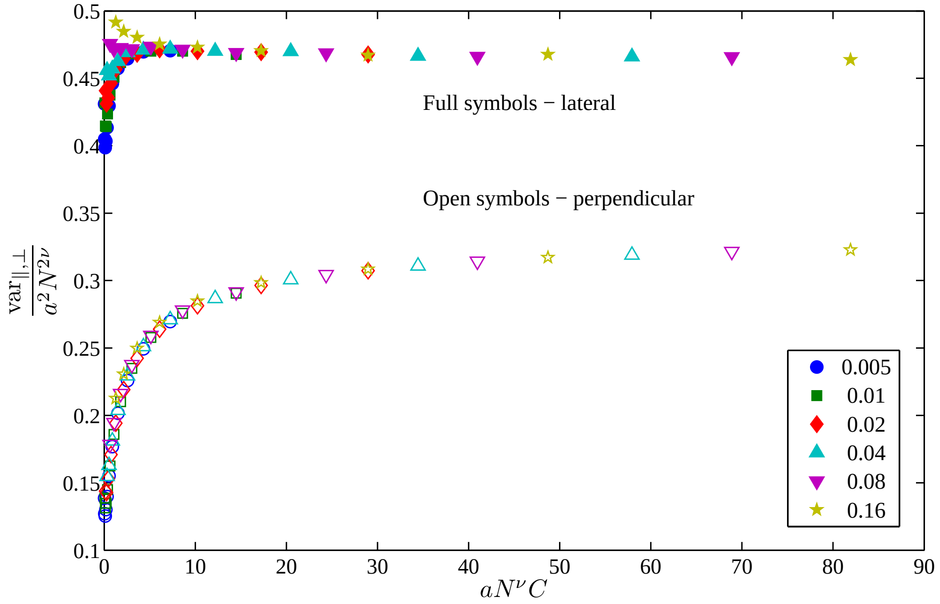

(a)

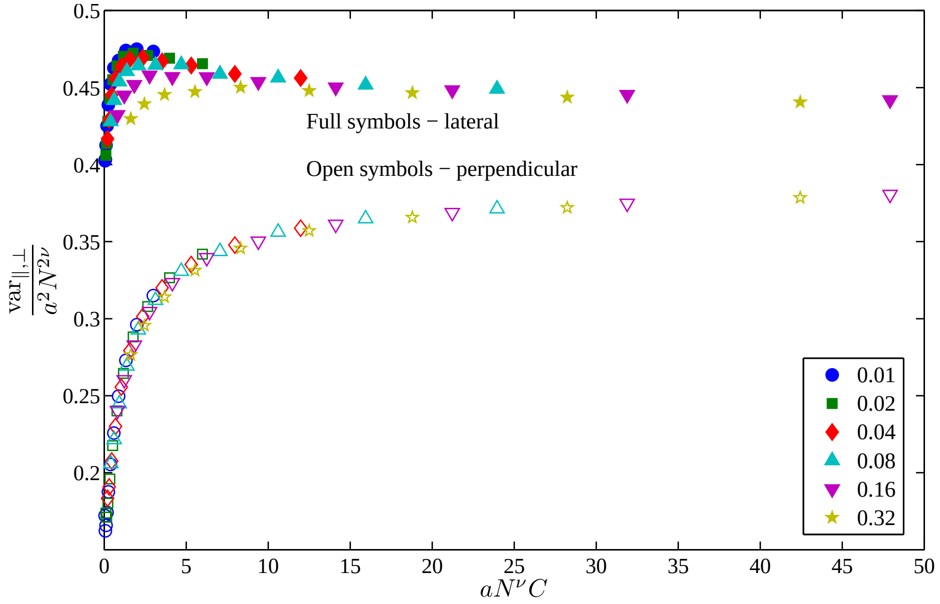

(b)

Figure 21: Scaling function for the linear response to force of (a) a two-dimensional SAW near a parabola and (b) a three-dimensional SAW near a paraboloid, for N ranging from 16 to 16384, coefficient C — from $0.005a^{-1}$ to $0.32a^{-1}$ (symbols indicate different C — see legend), and D equal to one lattice constant. Open (full) symbols indicate response to a perpendicular (lateral) force. Error bars are smaller than the size of the symbols.

5.5 Number of Configurations

We can derive a scaling assumption for $\frac{\mathcal{N}_{N,\text{parabola}}}{\mathcal{N}_N}$, the fraction of allowed walks given the constraint of the excluded parabola, using similar reasoning to that presented in Section 4.5 for circles or spheres. The analogous assumption here is:

$$\frac{\mathcal{N}_{N,\text{parabola}}}{\mathcal{N}_N} = (aC)^{\frac{\gamma_1-\gamma}{\nu}} \, \Phi\left(aN^{\nu}C\right). \tag{5.14}$$

However, in this case the scaling function is not expected to converge to a constant for $s \to \infty$, but to decay as a power law. In this limit we expect $\frac{\mathcal{N}_{N,\text{parabola}}}{\mathcal{N}_N} \sim N^{\gamma_{\text{line}}-\gamma}$ and therefore $\Phi(s) \sim s^{\frac{\gamma_{\text{line}}-\gamma}{\nu}}$.

The simulation results for RWs in two and three dimensions near an excluded parabola or paraboloid are shown in Fig. 22, which shows plots of $\frac{\mathcal{N}_{N,\text{parabola}}}{\mathcal{N}_N}(aC)^{\frac{\gamma-\gamma_1}{\nu}}$ as a function of $aN^{\nu}C$. As in Section 4.5, the results show quite good data collapse, though there are slight deviations from scaling.

In the limit of short walks we expect similar behavior to that obtained in Section 4.5, i.e. $\Phi(s \to 0) \sim s^{\frac{\gamma_1-\gamma}{\nu}}$, where for the RW model $\frac{\gamma_1-\gamma}{\nu} = -1$ in two and three dimensions. The simulation results match this value well: by using the extrapolation method described in Section 4.5 we obtain the exponents -0.98 and -0.95 for the two- and three-dimensional RW, respectively.

In the limit of long walks we expect $\Phi(s \to \infty) \sim s^{\frac{\gamma_{\text{line}}-\gamma}{\nu}}$. For the RW model $\frac{\gamma_{\text{line}}-\gamma}{\nu} = -\frac{1}{2}$ in $d = 2$ and zero (with logarithmic corrections) in $d = 3$. The simulation results show large deviations from these values: when a fit is performed for $s \geq 5$, the resulting exponents are -0.61 and -0.37 for the two- and three-dimensional RW, respectively.

Before discussing the reasons for this discrepancy, we first present the results for SAWs, shown in Fig. 23. These results show data collapse which is slightly poorer than the RW results. In the limit of short walks we expect $\Phi(s \to 0) \sim s^{\frac{\gamma_1-\gamma}{\nu}}$. The values obtained from the results are -0.52 and -0.77 in two and three dimensions respectively, in good agreement with the predicted values of -0.52 and -0.81.

Like the RW results, the SAW results fail to match predictions in the limit of long walks, where the predicted behavior is $\Phi(s \to \infty) \sim s^{\frac{\gamma_{\text{line}}-\gamma}{\nu}}$. In $d = 2$, $\frac{\gamma_{\text{line}}-\gamma}{\nu} \approx -0.21$

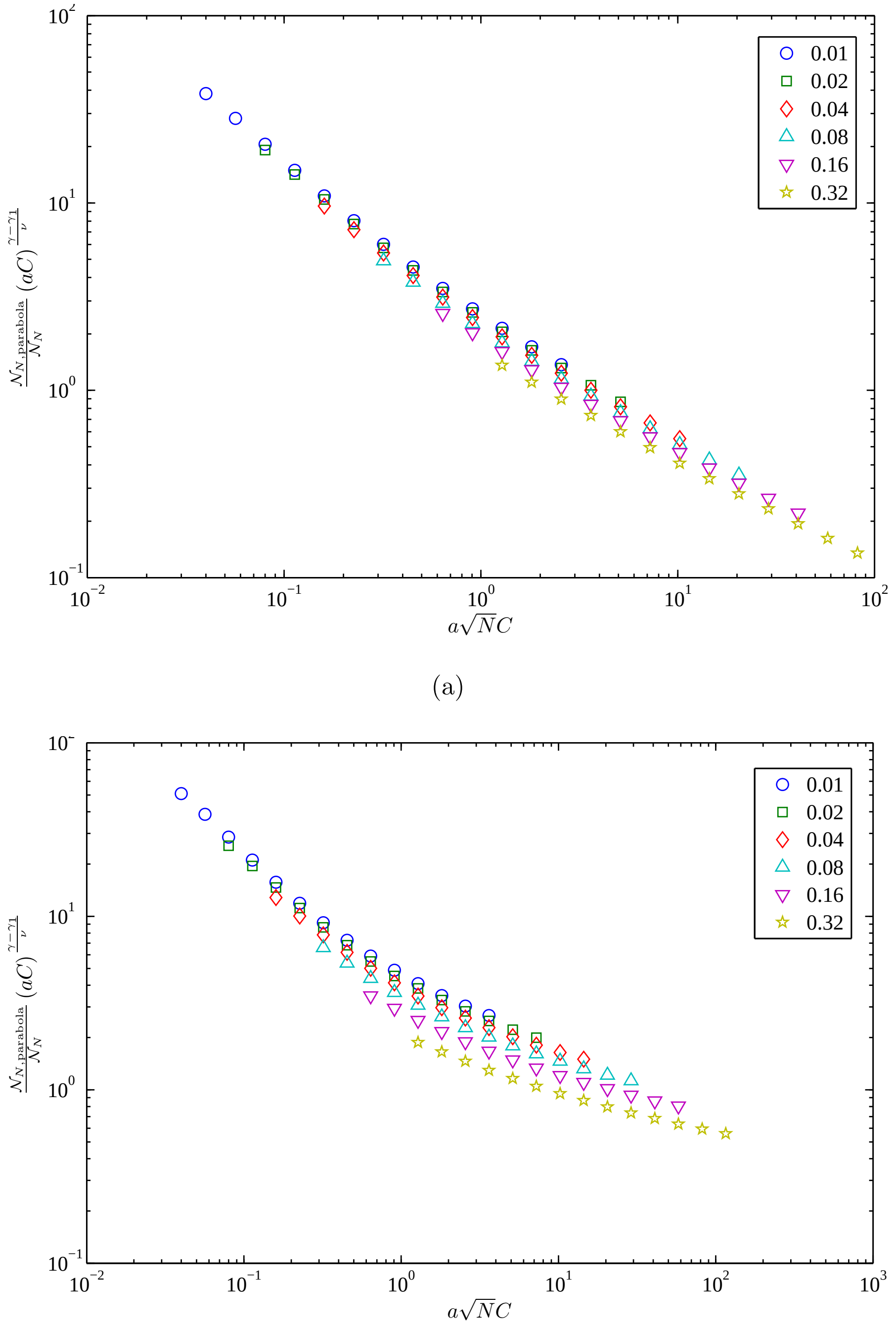

(a)

(b)

Figure 22: Scaling function for the fraction of allowed walks for (a) a two-dimensional RW near a parabola and (b) a three-dimensional RW near a paraboloid, for N ranging from 16 to 65536, coefficient C — from 0.01 to 0.32 inverse lattice constants (symbols indicate different values of C — see legend), and D equal to one lattice constant.

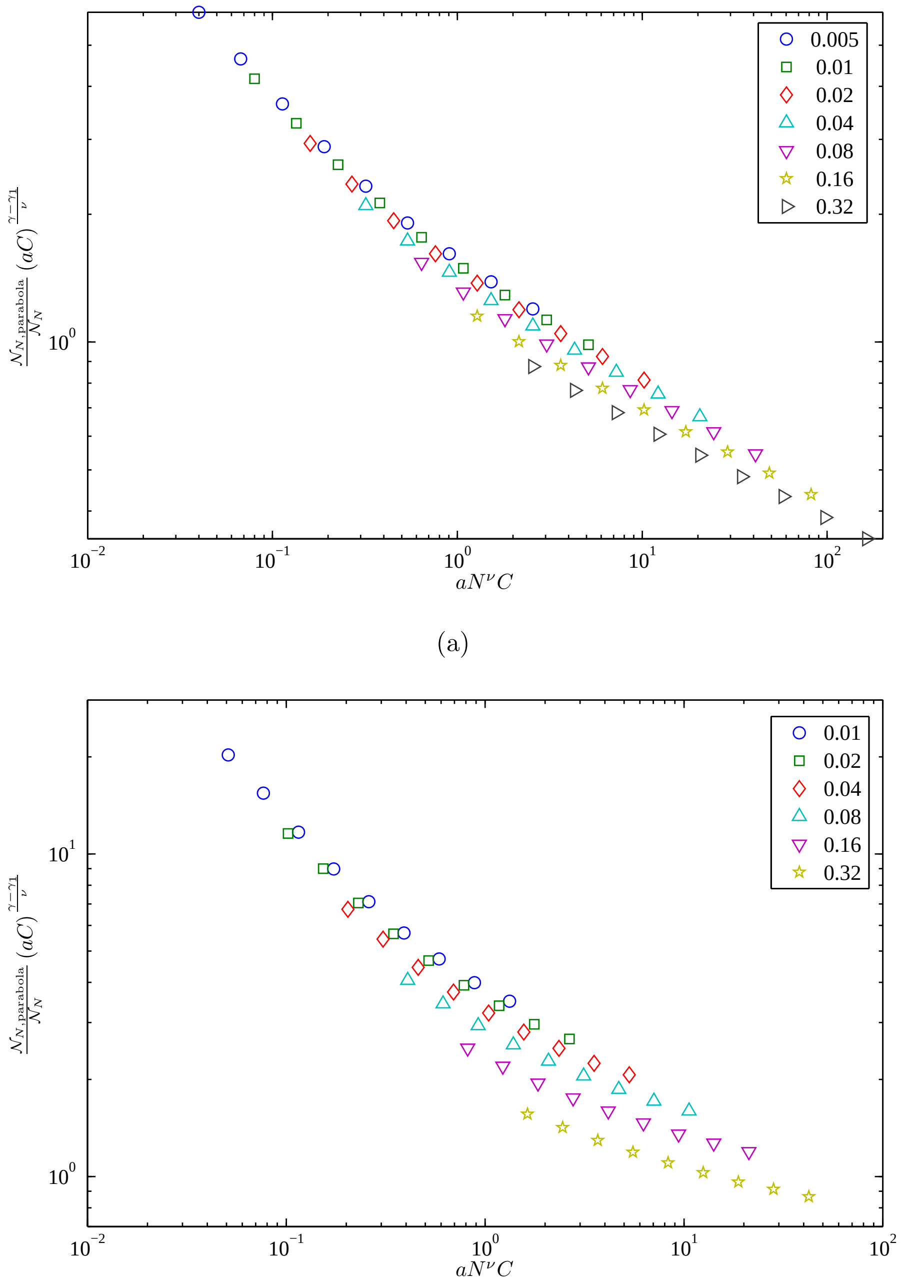

(a)

(b)

Figure 23: Scaling function for the fraction of allowed walks for (a) a two-dimensional SAW near a parabola and (b) a three-dimensional SAW near a paraboloid, for N ranging from 16 to 16384, coefficient C — from 0.005 to 0.32 inverse lattice constants (symbols indicate different values of C — see legend), and D equal to one lattice constant.

and the result of a fit for $s \geq 5$ gives an exponent of -0.27, while for $d = 3$ the predicted value is 0 and the fit gives an exponent of -0.29. This last result is in complete contradiction to our predictions.

In order to explain the unexpected results in the limit of long walks (for both RWs and SAWs), we describe the parabola using the two bounding geometries shown in Fig. 24. The first (inner) bound is a planar wedge ($d = 2$) or cone ($d = 3$) with an opening angle $\theta = 2\arcsin\left(\sqrt{\frac{1}{CR_0}}\right)$. The second (outer) bound is a semi-infinite rectangle ($d = 2$) or cylinder ($d = 3$) with width (diameter) $2W = 2\sqrt{\frac{R_0}{C}}$. The reasoning for these bounds is that the walk is only affected by the part of the parabola that is within a distance of approximately R_0 from the initial point of the walk.

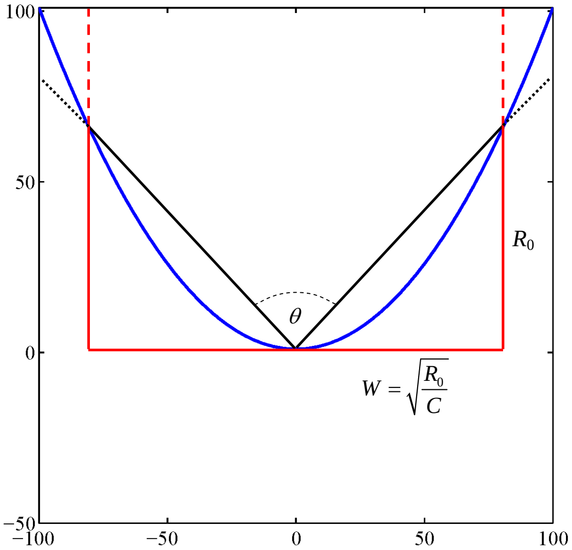

Figure 24: Geometrical bounds for the parabola in $d = 2$: planar wedge of opening angle θ and rectangle of width $2W$.

The angle θ which defines the inner bound decreases as $\frac{1}{\sqrt{s}}$, and therefore in the limit of long walks the inner bound should reproduce the behavior of a walk near a line. For instance, the exact formula for a two-dimensional SAW near a planar wedge of opening angle θ is

$$\gamma(\theta) = \frac{\pi}{2\pi - \theta}\gamma_1 - \left(\frac{\pi}{2\pi - \theta} - 1\right)\left(\nu + \frac{\gamma}{2}\right). \tag{5.15}$$

Inserting the appropriate values of the exponents into (5.15), and using $\theta \approx \frac{2}{\sqrt{s}}$, we obtain

$$\gamma(s) \approx \gamma_{\text{line}} - \frac{15}{64\pi\sqrt{s}}. \tag{5.16}$$

For the higher values of s used in our work ($s \approx 45$), $\gamma(s)$ is within 3% of γ_{line}.

If we consider the outer bound of the parabola, we can formulate the following scaling assumption for the number of walks near a rectangle of width $2W$ (numerical results for this geometry are given in Appendix B):

$$\frac{\mathcal{N}_{N,W}}{\mathcal{N}_N} = \left(\frac{W}{a}\right)^{\frac{\gamma_1-\gamma}{\nu}} \Phi\left(\frac{aN^\nu}{W}\right). \tag{5.17}$$

In the limit of short walks we expect $\Phi(s) \sim s^{\frac{\gamma_1-\gamma}{\nu}}$, eliminating the dependence on W. In the limit of long walks we expect $\Phi(s) \sim s^{\frac{\gamma_{\text{line}}-\gamma}{\nu}}$, giving us

$$\frac{\mathcal{N}_{N,W}}{\mathcal{N}_N} \sim \left(\frac{W}{a}\right)^{\frac{\gamma_1-\gamma_{\text{line}}}{\nu}} N^{\gamma_{\text{line}}-\gamma}. \tag{5.18}$$

Inserting the value $W = \sqrt{\frac{aN^\nu}{C}}$ into Eq. 5.18, we arrive at

$$\frac{\mathcal{N}_{N,W=\sqrt{\frac{aN^\nu}{C}}}}{\mathcal{N}_N} \sim (aC)^{-\frac{1}{2\nu}(\gamma_{\text{line}}-\gamma_1)} N^{\frac{\gamma_{\text{line}}+\gamma_1}{2}-\gamma}. \tag{5.19}$$

This result indicates that for the outer bound of the parabola, we must replace γ_{line} with $\frac{\gamma_{\text{line}}+\gamma_1}{2}$.

Table 1 compares the numerical results with the predicted values of the inner bound (γ_{line}) and the outer bound $\left(\frac{\gamma_{\text{line}}+\gamma_1}{2}\right)$. Our results fall between these two bounds, but due to the scattering of the data points it is difficult to determine whether this is the result of a slow crossover, or if there is indeed a new exponent involved.

Type of Walk	$\gamma_{\text{numerical}}$	γ_{line}	$\frac{\gamma_{\text{line}}+\gamma_1}{2}$
Two-dimensional RW	0.70	$\frac{3}{4}$	$\frac{5}{8} \approx 0.63$
Three-dimensional RW	0.82	1	$\frac{3}{4}$
Two-dimensional SAW	1.14	$\frac{19}{16} \approx 1.19$	$\frac{137}{128} \approx 1.07$
Three-dimensional SAW	0.99	1.16	0.92

Table 1: Comparison of numerical results for the number of walks near a parabola with predictions for the inner and outer bounds.

6 Conclusions and Future Prospects

We have investigated two lattice models of polymers attached by one end to an impenetrable probe. Three main properties of the polymers were studied: the separation of the endpoint from the probe, the response to an applied force and the number of available configurations. These properties were put into a scaling form, taking into consideration the mean size of the polymer and the length scale of the probe. The values of the properties were calculated for a broad range of these parameters using Monte Carlo simulation.

The behavior of the scaling functions for these properties in the two limiting cases — polymers much longer or much shorter than the probe length scale — were compared to theoretical predictions. On the whole, the results matched our predictions. The behavior of one property — the separation of the polymer endpoint from a circle in two dimensions — could not be predicted beforehand, since there is no consensus in the current literature. We were unable to make a clear determination regarding this property, though we were able to rule out a power law behavior for this property.

Possibly the most interesting finding was the non-monotonic behavior of the scaling function for the response to a lateral force: this scaling function showed a maximum when the polymer size and the probe length scale are of the same order (this was most noticeable for the circular geometry). It should be noted that there have been very few single-molecule experiments in which a lateral force is applied to the molecule [73].

The number of configurations of a polymer near a parabola showed unexpected behavior at the limit of polymers much longer than the length scale of the parabola. We attempted to explain this discrepancy by using two geometric bounds for the parabola and comparing the numerical results to those expected for these bounds. We were unable to verify whether the unexpected behavior indicates the appearance of a new exponent or whether it is simply due to a slow crossover.

In several instances the discreteness of the lattice affected the numerical results. Therefore an interesting comparison could be made to similar simulations in a continuum model, where it is more likely that the predicted behavior will be reproduced precisely. It is also possible to consider a more limited ensemble, that of all configurations of a given length *with a fixed end-to-end vector*. Though different ensembles should give the same properties in equilibrium, different results might be obtained in different ensembles for large deviations from equilibrium.

Although single-molecule experiments focus mainly on the regime of large forces, where the models used in this work are inapplicable, the results of the work could become more relevant as the application and measurement of lower forces (or the study of larger polymers) becomes possible. Our results show that at the limit of low forces, probes exert an important influence on polymers attached to them, and theoretical interpretation of the experimental results should account for such factors.

A Dynamic Monte Carlo Simulation

In this Appendix we discuss in greater detail the Monte Carlo methods used in our work to study SAWs. These methods are described in general terms in Section 2.5.

A.1 Definitions

Monte Carlo methods can be classified as either *static* or *dynamic*. Static methods generate each configuration independently from previous ones, with a probability equal to the desired probability distribution π (π_i is the probability associated with walk i in the ensemble). Dynamic methods generate a sequence of correlated configurations, using a Markov process which has the desired probability distribution π as its unique equilibrium distribution. The Markov process is defined as a probability matrix $P(i \to j)$, for the transitions from one walk (i), to the next walk (j):

$$P(i \to j) = \Pr\{\omega^{[t+1]} = j | \omega^{[t]} = i\} \quad (t \geq 0, i, j \in \Omega), \tag{A.1}$$

where $\omega^{[t]}$ is the walk produced at step t, and Ω (in our work) is the set of all self-avoiding walks of a given length.

It can be shown [74] that a Markov process has π as its unique equilibrium distribution if it satisfies two conditions:

1. *Ergodicity*: each state can eventually be reached from any other state.
2. *Detailed Balance*: For each pair $i, j \in S$, $\pi_i P(i \to j) = \pi_j P(j \to i)$. Since π in our case is a uniform distribution (each walk has equal weight), this reduces to the condition that the probability for each transition $i \to j$ must be equal to the probability of the inverse transition $j \to i$.

The process can be initialized with an arbitrary configuration and run for a sufficiently long time to "thermalize", prior to observing the system. Equivalently, it can be started with a configuration from the equilibrium distribution, e.g. (for a SAW) one obtained via the dimerization algorithm. The canonical average of any observable $A_t \equiv A\left(\omega^{[t]}\right)$ is approximated by a simple arithmetic mean:

$$\langle A \rangle \approx \bar{A} \equiv \frac{1}{n} \sum_{t=1}^{n} A_t, \tag{A.2}$$

where n is the number of steps performed after thermalization.

Since the successive states $\omega^{[1]}, \omega^{[2]}, \ldots$ of the Markov chain are highly correlated, the variance of this estimate is higher than in independent sampling. In order to measure these correlations, we define the *unnormalized autocorrelation function*:

$$C_{AA}(t) \equiv \langle A_s A_{s+t} \rangle - \langle A \rangle^2, \tag{A.3}$$

and the *normalized autocorrelation function*:

$$\rho_{AA}(t) \equiv C_{AA}(t)/C_{AA}(0). \tag{A.4}$$

These functions decay at a time-scale corresponding to the *integrated autocorrelation time* $\tau_{\text{int},A}$, defined as:

$$\tau_{\text{int},A} = \frac{1}{2} \sum_{t=-\infty}^{\infty} \rho_{AA}(t) = \frac{1}{2} + \sum_{t=1}^{\infty} \rho_{AA}(t) \tag{A.5}$$

(The factor of $\frac{1}{2}$ is a matter of convention; if $\rho_{AA}(t) \sim e^{-|t|/\tau}$, with $\tau \gg 1$, then $\tau_{\text{int},A} \approx \tau$). It is this quantity that controls the statistical error [38]:

$$\operatorname{var}\left(\bar{A}\right) \approx \frac{1}{n}(2\tau_{\text{int},A})C_{AA}(0). \tag{A.6}$$

Thus, the number of "effectively independent configurations" in a run of length n is roughly $\frac{n}{2\tau_{\text{int},A}}$.

A.2 The Pivot Algorithm

The method used in our work to study self-avoiding walks is the pivot algorithm [37, 38]. Its general description can be found in Section 2.5.2. Starting with a given configuration, a random site of the walk is selected as a 'pivot site', which divides the walk into two sections. A symmetry operation of the lattice (either rotation or reflection) is chosen at random and applied to one section of the walk[1], with the pivot site as the origin of the symmetry operation. If the resulting walk is self-avoiding, it is accepted, otherwise the original walk is counted again.

---

[1] In order to keep one end of the walk at the origin of coordinates, the symmetry operation is always applied to the section of the walk which does not contain this end.

The algorithm described above does not include an impenetrable probe. In order to take the probe into account, the lattice is divided into two domains — inside and outside the probe — and two variants of the algorithm are used:

1. The first variant is used to calculate the number of SAWs of a given length which do not penetrate the probe. We use the method described above, and check after each iteration whether all points of the resulting walk are outside the domain of the probe. The mean value of this 'success rate' is the fraction of SAWs of a given length, which do not penetrate the probe.
2. The second variant is used to calculate the distribution of the endpoint of the walk. In this variant we check whether the walk resulting from the pivot move penetrates the probe, and reject it if it does (this condition is added to the self-avoidance condition). The endpoint positions of the allowed walks are used to calculate the distribution.

It has been shown that these variants of the algorithm are ergodic [75], so all allowed configurations of the walk are explored by the algorithm. However, according to [76] the pivot algorithm is inefficient for walks in the presence of impenetrable surfaces, since the part of the walk nearest the surface will rarely be updated and the correlation time will increase very rapidly with the length of the walk. We expect the biggest impact to be on observables that depend strongly on the behavior of the walk near the excluded surface (for example, the orientation of the first step of the walk). In Section A.2.2 we discuss the effect of the impenetrable surface on the efficiency of the algorithm for the different observables, and show that this problem is restricted to observables which depend on local properties of the walk.

A.2.1 Thermalization

The simulations of short walks ($N \leq 4096$) were initialized using the dimerization algorithm (when necessary, using a variant which produces walks that do not penetrate the probe region). Longer walks were initialized with a straight line configuration, and thermalized before recording the observables.

It is possible to visually examine the effect of thermalization, by dividing a run of 10^6 iterations (beginning from a straight line configuration) into "batches" of 10^4 consecutive observations, and looking at the means of the squared end-to-end distance and the variance of the endpoint position in each batch. The initial batches show significantly higher values than the rest for these observables, since they are maximal for configurations which are nearly straight. The batches corresponding to observations after thermalization should show statistically similar values. The results are shown in Fig. 25, for two representative geometries: a two-dimensional SAW near a parabola with coefficient $C = \frac{0.005}{a}$, and a three-dimensional SAW near a sphere of radius $R = 192a$. Both walks are 16,384-steps long: the longest SAWs studied in this work.

From the results it can be seen that for a two-dimensional SAW, the initial bias has disappeared after about 200,000 iterations (20 batches). This value agrees with the one used by the authors of [38] for walks of up to 10,000 steps. We chose the blanket rule of discarding the first 300,000 iterations when beginning with a straight line configuration; this rule is applicable to three-dimensional walks and to shorter walks, since their thermalization time is shorter.

A.2.2 Autocorrelation Time

A "natural" estimate for the integrated autocorrelation time $\tau_{\text{int},A}$ of an observable A is obtained from Eq. (A.5):

$$\tau_{\text{int},A} = \frac{1}{2} \sum_{t=-(n-1)}^{n-1} \rho_{AA}(t), \tag{A.7}$$

where n is the sample size and $\rho_{AA}(t)$ is calculated from the samples. However, this is not a useful estimator, since it has a variance which does not go to zero as the sample size n goes to infinity [77]. The reason is that for $|t| \gg \tau$, $\rho_{AA}(t)$ contains mostly "noise", and when many (order n) such terms are summed, the noise adds up to a variance of order 1. The solution is to impose a cutoff value, or "window", M, and use the estimate [38]

$$\tau_{\text{int},A} = \frac{1}{2} \sum_{t=-M}^{M} \rho_{AA}(t). \tag{A.8}$$

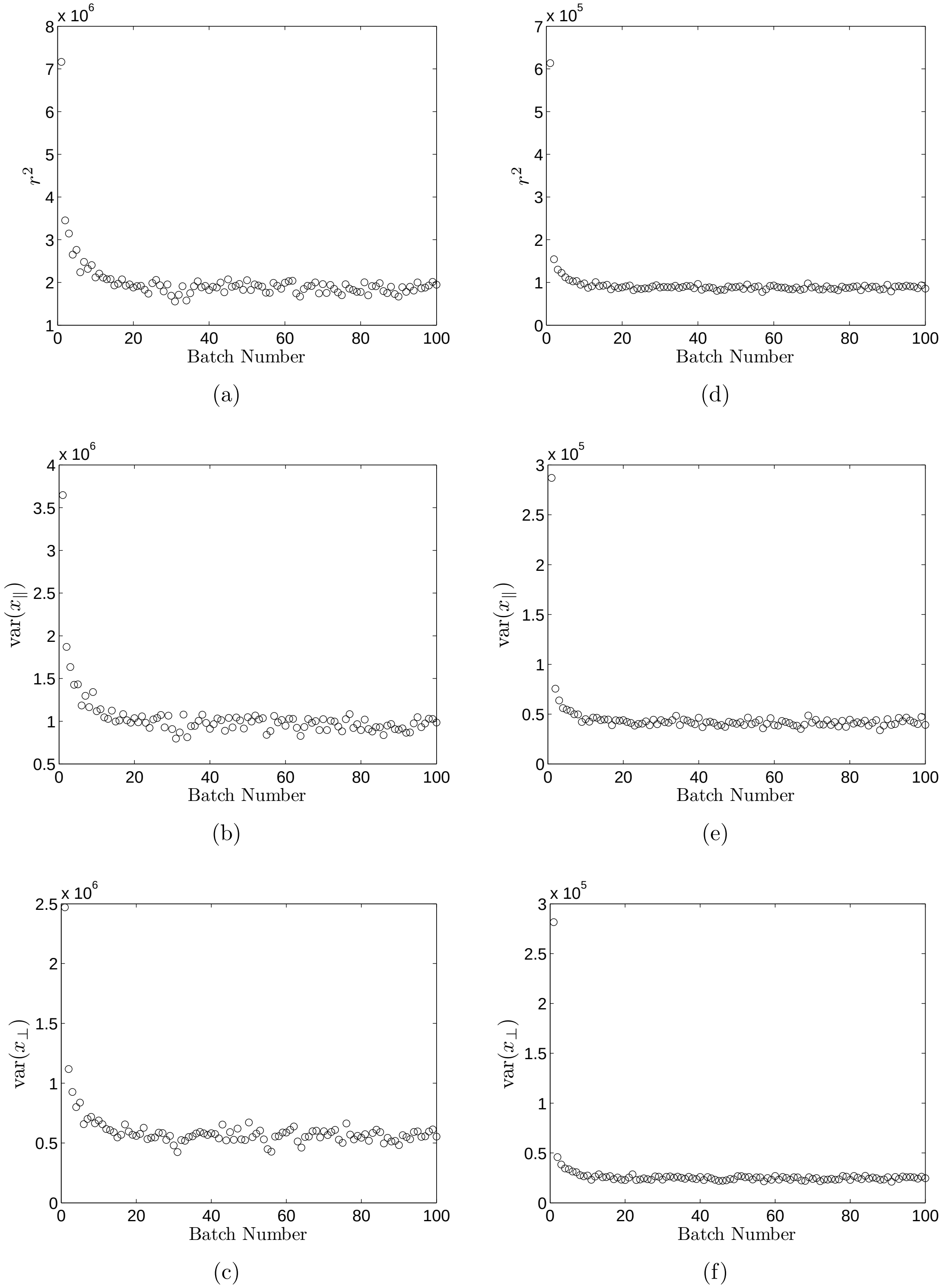

Figure 25: Means of consecutive observables over a batch: (a-c) a two-dimensional SAW near a parabola with coefficient $\frac{0.005}{a}$, and (d-f) a three-dimensional SAW near a sphere of radius $192a$.

This allows us to keep most of the “signal” and discard most of the noise. However, this cutoff introduces a bias to the estimate, due to the truncation of the sum:

$$\text{bias}(\tau_{\text{int},A}) \approx -\frac{1}{2} \sum_{|t|>M} \rho_{AA}(t). \tag{A.9}$$

The variance of the estimate of τ_{int} also depends on the cutoff value [38]:

$$\text{var}\left(\tau_{\text{int},A}\right) \approx \frac{2(2M+1)}{n} \tau_{\text{int},A}^2. \tag{A.10}$$

We see that there is a trade-off in the choice of M, between bias and variance — the bias can be made small by taking M large enough so that $\rho_{AA}(t)$ is negligible for $|t| > M$, while the variance can be kept small by taking M no larger then necessary, consistent with this constraint. In order to find the optimal cutoff value we use an “automatic windowing” algorithm described in [78], which minimizes the sum of the absolute values of the bias (systematic error) and the statistical error.

The integrated correlation times for some of the configurations studied are given in tables 2 and 3. The autocorrelation time for r^2 increases slowly with the length of the walk (in [38], the authors find $\tau_{\text{int}} \sim N^{0.2}$ for global observables). In addition, the dependence of this autocorrelation time on the length scale of the impenetrable probe is rather weak, generally increasing with the size of the probe (increasing radius or decreasing parabola coefficient). We can conclude that this global observable is not greatly affected by the inefficiency associated with the use of the pivot algorithm in the presence of an impenetrable surface, which was discussed in the beginning of this section.

In contrast, the autocorrelation time for the fraction of walks that do not penetrate the probe increases far more rapidly with N. For example, for a two-dimensional SAW near a circle of radius $6a$, the autocorrelation time increases from 150 for walks of length 512, to 960 for walks of length 4096, rising almost linearly with N. The autocorrelation time for this observable also shows a strong dependence on the size of the excluded region. Both these characteristics indicate a dependence on local properties — probably due to the fact that the orientation of the first few steps plays a large part in determining whether the walk penetrates the probe or not.

Table 2: Autocorrelation times for two-dimensional SAWs of length N near circles of radii R (in lattice constants) or parabolas with coefficient C (in inverse lattice constants)

(a) τ_{int} for r^2 of a SAW near a circle ($d = 2$).

R N	$6a$	$12a$	$24a$	$48a$	$96a$	$192a$
512	11 ± 0.6	13.2 ± 0.8	14.3 ± 0.9	15.5 ± 1	14.6 ± 0.9	18.3 ± 1.2
1024	13.6 ± 0.8	13.8 ± 0.8	14.5 ± 0.9	16.1 ± 1	19.3 ± 1.4	18.2 ± 1.2
2048	16.5 ± 1.1	14.8 ± 0.9	15.7 ± 1	16.9 ± 1.1	18.8 ± 1.3	21.2 ± 1.5
4096	20.4 ± 1.5	18.7 ± 1.3	20.4 ± 1.5	16.6 ± 1.1	20.7 ± 1.5	23.5 ± 1.8

(b) τ_{int} for r^2 of a SAW near a parabola ($d = 2$).

C N	$\frac{0.005}{a}$	$\frac{0.01}{a}$	$\frac{0.02}{a}$	$\frac{0.04}{a}$	$\frac{0.08}{a}$	$\frac{0.16}{a}$
512	18.1 ± 1.2	14.7 ± 0.9	15.6 ± 1	13.5 ± 0.8	15.2 ± 1	14.1 ± 0.9
1024	17.7 ± 1.2	19.2 ± 1.3	18.7 ± 1.3	17.9 ± 1.2	16.1 ± 1	17.1 ± 1.1
2048	18.3 ± 1.2	20.5 ± 1.5	17 ± 1.1	19.7 ± 1.4	17.6 ± 1.2	18.6 ± 1.3
4096	21.6 ± 1.6	20.6 ± 1.5	24.3 ± 1.9	25.9 ± 2.1	21.3 ± 1.6	22 ± 1.6

(c) τ_{int} for the fraction of SAWs that do not penetrate a circle ($d = 2$).

R N	$6a$	$12a$	$24a$	$48a$	$96a$	$192a$
512	150 ± 10	117 ± 7	91 ± 5	75 ± 3	64 ± 3	57 ± 2
1024	300 ± 20	220 ± 20	180 ± 10	128 ± 7	98 ± 5	82 ± 4
2048	570 ± 60	420 ± 40	300 ± 20	210 ± 10	150 ± 10	117 ± 7
4096	960 ± 130	740 ± 90	560 ± 60	430 ± 40	290 ± 20	200 ± 10

(d) τ_{int} for the fraction of SAWs that do not penetrate a parabola ($d = 2$).

C N	$\frac{0.005}{a}$	$\frac{0.01}{a}$	$\frac{0.02}{a}$	$\frac{0.04}{a}$	$\frac{0.08}{a}$	$\frac{0.16}{a}$
512	62 ± 3	70 ± 3	79 ± 4	89 ± 4	99 ± 5	105 ± 6
1024	92 ± 5	110 ± 6	130 ± 10	150 ± 10	160 ± 10	180 ± 10
2048	130 ± 10	160 ± 10	190 ± 10	220 ± 20	240 ± 20	270 ± 20
4096	230 ± 20	300 ± 30	340 ± 30	370 ± 30	430 ± 40	450 ± 50

Table 3: Autocorrelation times for SAWs of length N near spheres of radii R (in lattice constants) or paraboloids with coefficient C (in inverse lattice constants)

(a) τ_{int} for r^2 of a three-dimensional SAW near a sphere.

R N	$6a$	$12a$	$24a$	$48a$	$96a$	$192a$
512	5.5± 0.2	4.5± 0.2	3.5± 0.1	3.2± 0.1	3.3± 0.1	3.4± 0.1
1024	6.3± 0.3	5.6± 0.2	4.5± 0.2	3.8± 0.1	3.5± 0.1	3.6± 0.1
2048	7.5± 0.3	6.7± 0.3	5.3± 0.2	4.6± 0.2	4.1± 0.1	3.9± 0.1
4096	8.2± 0.4	7.5± 0.4	6.7± 0.3	5.7± 0.2	4.6± 0.2	4.1± 0.1

(b) τ_{int} for r^2 of a SAW near a paraboloid ($d = 3$).

C N	$\frac{0.005}{a}$	$\frac{0.01}{a}$	$\frac{0.02}{a}$	$\frac{0.04}{a}$	$\frac{0.08}{a}$	$\frac{0.16}{a}$
512	3.3± 0.1	3.3± 0.1	3.3± 0.1	3.7± 0.1	4.1± 0.1	4.3± 0.2
1024	3.5± 0.1	3.6± 0.1	3.9± 0.1	4.3± 0.2	4.8± 0.2	5.2± 0.2
2048	4.1± 0.1	4.3± 0.2	4.5± 0.2	4.9± 0.2	5.3± 0.2	5.7± 0.2
4096	4.4± 0.2	4.8± 0.2	5.3± 0.2	5.6± 0.2	6.1± 0.3	6.6± 0.3

(c) τ_{int} for the fraction of SAWs that do not penetrate a sphere ($d = 3$).

R N	$6a$	$12a$	$24a$	$48a$	$96a$	$192a$
512	111± 6	74± 3	52± 2	40± 1	34± 1	31± 1
1024	220± 20	140± 10	94± 5	66± 3	50± 2	42± 2
2048	340± 30	200± 10	125± 7	89± 4	65± 3	54± 2
4096	820± 100	480± 50	270± 20	159± 10	107± 6	77± 4

(d) τ_{int} for the fraction of SAWs that do not penetrate a paraboloid.

C N	$\frac{0.005}{a}$	$\frac{0.01}{a}$	$\frac{0.02}{a}$	$\frac{0.04}{a}$	$\frac{0.08}{a}$	$\frac{0.16}{a}$
512	34± 1	39± 1	47± 2	60± 3	76± 4	96± 5
1024	48± 2	62± 3	80± 4	103± 6	134± 8	180± 10
2048	63± 3	79± 4	101± 5	131± 8	170± 10	230± 20
4096	99± 5	134± 8	180± 10	260± 20	370± 30	510± 50

Fig. 26 shows the normalized autocorrelation function for one geometry. From this figure it is clear that the approximation of the autocorrelation function as an exponentially decaying function is indeed only an approximation, though it is valid for a wide range of time-steps t (the function is approximately exponentially decaying up to $10t$).

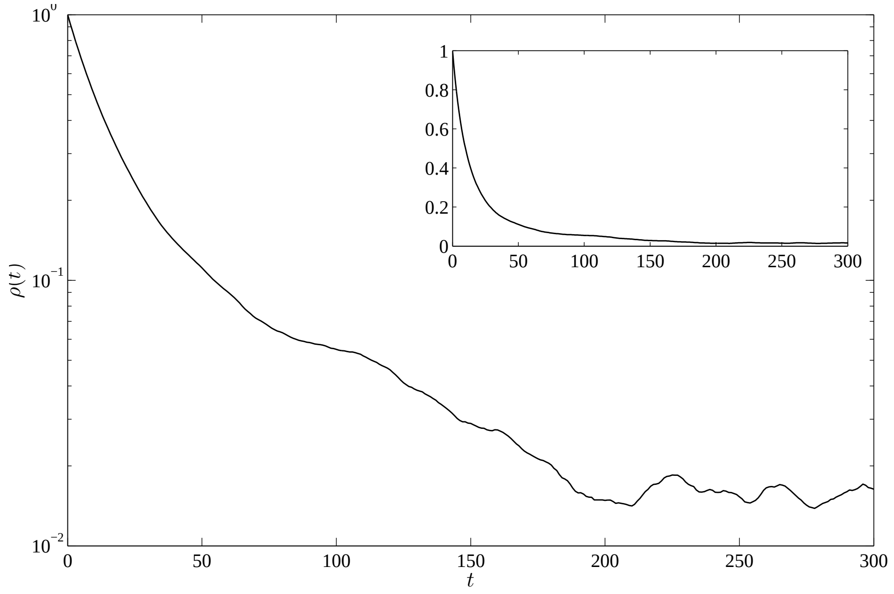

(a)

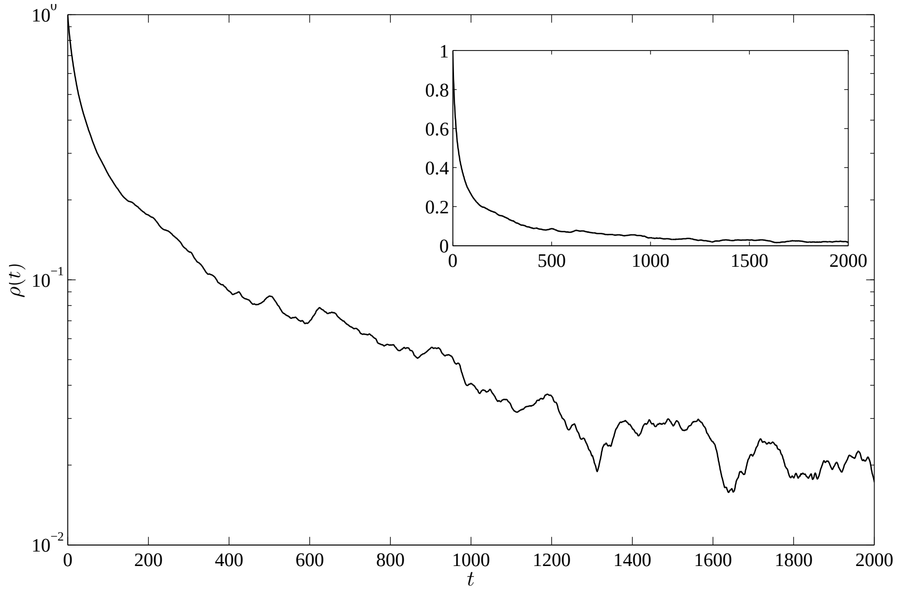

(b)

Figure 26: Normalized autocorrelation function of: (a) squared end-to-end distance and (b) fraction of walks which do not penetrate the probe, for a 2048-step two-dimensional SAW near a circle of radius $192a$. The corresponding values of τ_{int} are (a) 23 and (b) 130. Main figures show a semi-log plot, insets show a linear plot.

B Walks Near an Excluded Rectangle

In this Appendix we summarize the results obtained for the number of configurations of walks near an excluded semi-infinite rectangle (cylinder in $d = 3$) of width (diameter) $2W$. We denote this $\mathcal{N}_{N,W}$. We use the following scaling assumption:

$$\frac{\mathcal{N}_{N,W}}{\mathcal{N}_N} = N^{\gamma_1-\gamma}\Phi\left(\frac{aN^\nu}{W}\right). \tag{B.1}$$

In the limit $aN^\nu \ll W$ we expect the scaling function to be constant, giving the behavior of a walk near wall: $\frac{\mathcal{N}_{N,W}}{\mathcal{N}_N} \sim N^{\gamma_1-\gamma}$. At the opposite limit we expect $\Phi(s \to \infty) \sim s^{\frac{\gamma_{\text{line}}-\gamma_1}{\nu}}$, giving $\frac{\mathcal{N}_{N,W}}{\mathcal{N}_N} \sim N^{\gamma_{\text{line}}-\gamma}$.

The numerical results for RWs and SAWs in two and three dimensions are given in Figs. 27 and 28, which show plots of $\frac{\mathcal{N}_{N,W}}{\mathcal{N}_N}N^{\gamma-\gamma_1}$ as a function of $\frac{aN^\nu}{W}$. The results display excellent data collapse (better than that observed in Sections 4.5 and 5.5).

As expected, the scaling functions are constant at low values of the scaling variable s, and show a clear crossover at $s \approx 1$ to a power law behavior. We can extrapolate the exponent γ_{line} from this power law: the results are summarized in Table 4 and compared to the theoretical predictions. The numerical results for the two-dimensional models are in excellent agreement with the theoretical values, while the results in $d = 3$ (where we expect γ_{line} to be equal to the bulk value γ) are slightly lower than the theoretical values.

Type of Walk	$\gamma_{\text{line,theoretical}}$	$\gamma_{\text{rectangle,numerical}}$
Two-dimensional RW	$\frac{3}{4}$	0.74
Three-dimensional RW	1	0.93
Two-dimensional SAW	$\frac{19}{16} \approx 1.19$	1.18
Three-dimensional SAW	1.16	1.10

Table 4: Comparison of theoretical predictions for the exponent γ_{line} with numerical results for walks near a semi-infinite rectangle or cylinder.

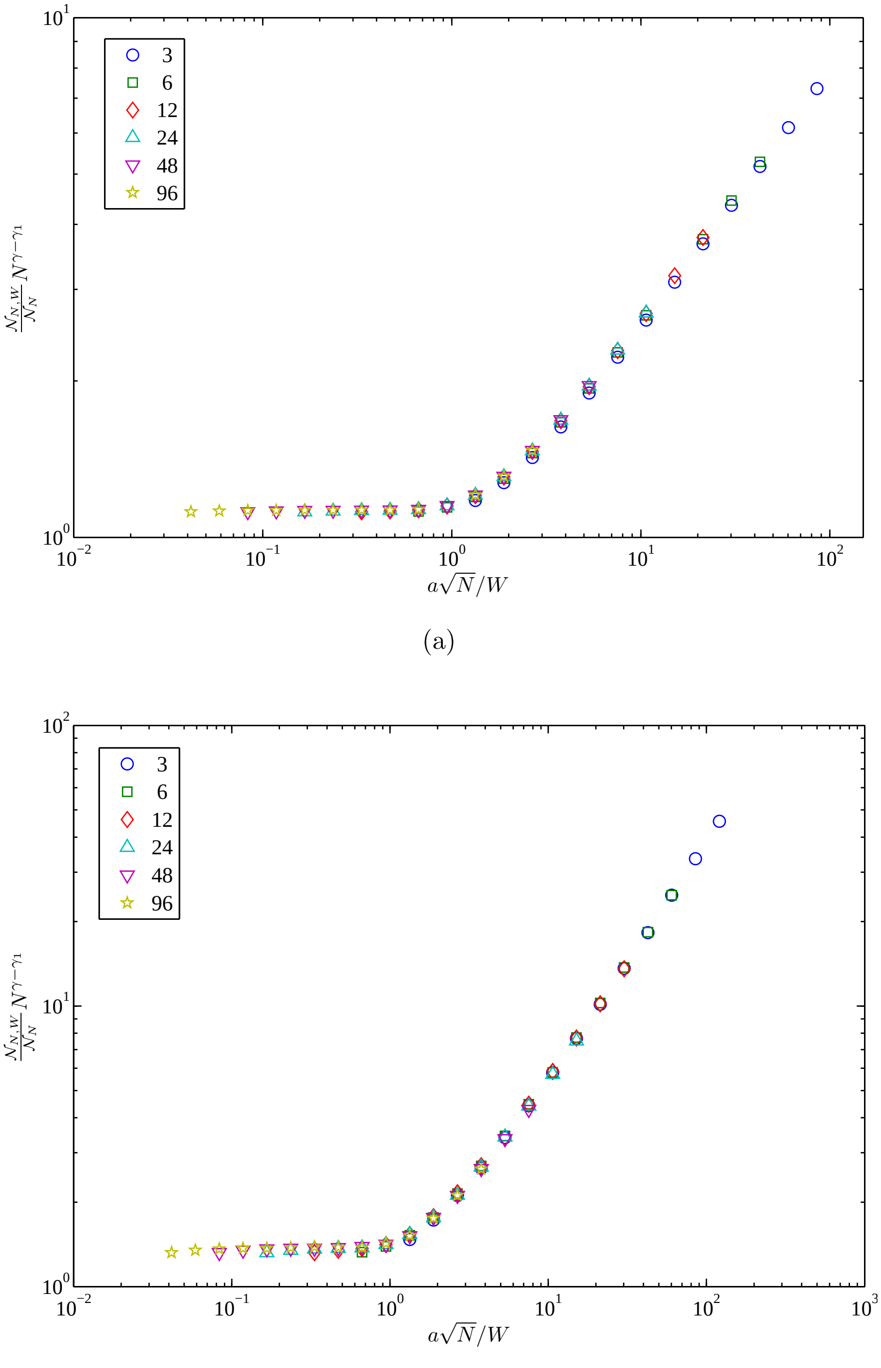

(a)

(b)

Figure 27: Scaling function for the fraction of allowed walks for (a) a two-dimensional RW near a rectangle of width $2W$ and (b) a three-dimensional RW near a cylinder of diameter $2W$, for N ranging from 16 to 131072, W — from 3 to 96 lattice constants (symbols indicate different values of W — see legend), and D equal to one lattice constant.

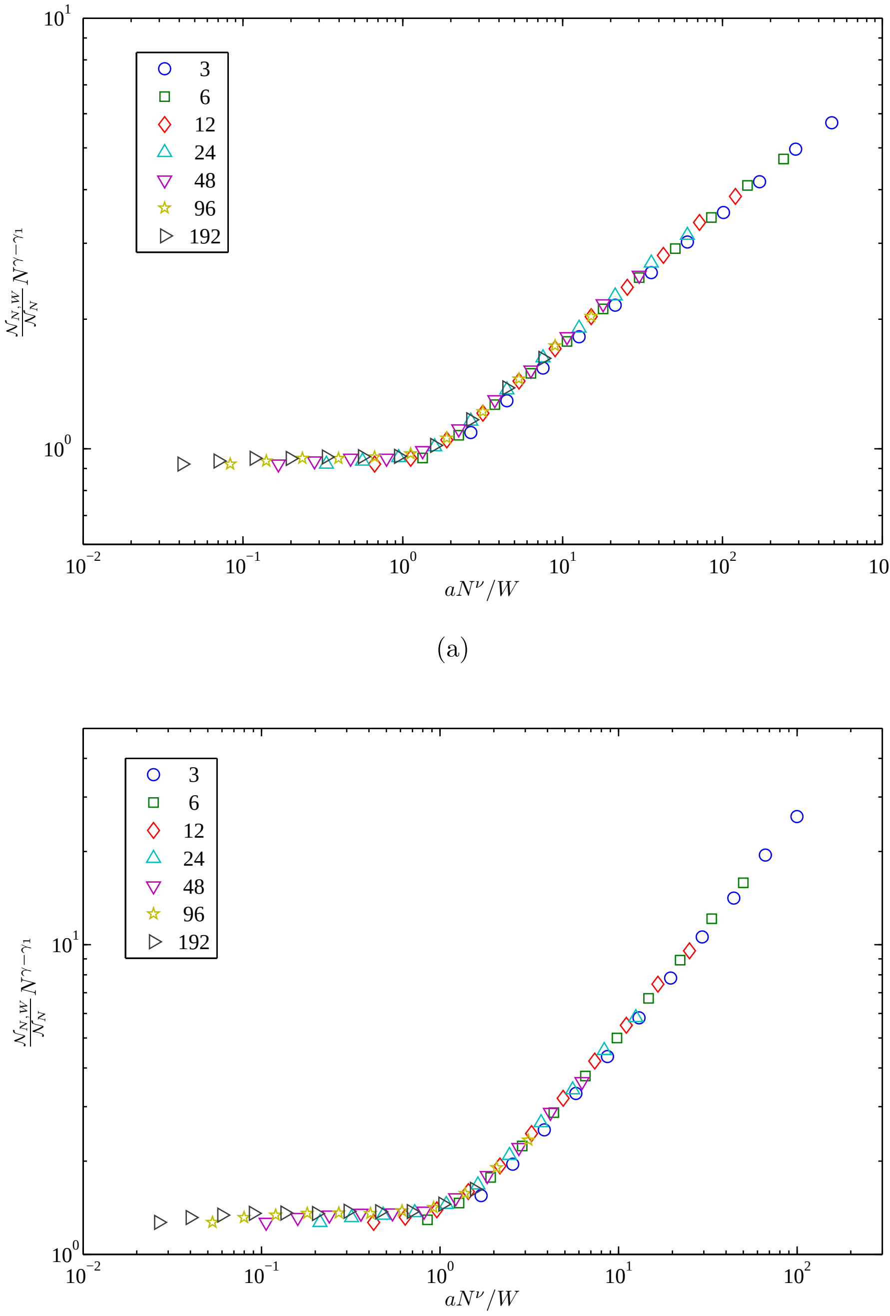

(a)

(b)

Figure 28: Scaling function for the fraction of allowed walks for (a) a two-dimensional SAW near a rectangle of width $2W$ and (b) a three-dimensional SAW near a cylinder of diameter $2W$, for N ranging from 16 to 16384, W — from 3 to 192 lattice constants (symbols indicate different values of W — see legend), and D equal to one lattice constant.

References

[1] C. Bustamante, J. C. Macosko and G. J. L. Wuite, *Nat. Rev. Mol. Cell. Biol.* **1**, 130 (2000).

[2] C. Bustamante, Z. Bryant and S. B. Smith, *Nature* **421**, 423 (2003).

[3] M. S. Kellermayer, *Physiol. Meas.* **26**, R119 (2005).

[4] K. Neuman, T. Lionnet and J.-F. Allemand, *Ann. Rev. Mater. Res.* **37**, 33 (2007).

[5] A. A. Deniz, S. Mukhopadhyay and E. A. Lemke, *J. R. Soc. Interface* **5**, 15 (2008).

[6] T. E. Fisher, P. E. Marszalek, A. F. Oberhauser, M. Carrion-Vazquez and J. M. Fernandez, *J. Physiol.* **520**, 5 (1999).

[7] A. Kishino and T. Yanagida, *Nature* **334**, 74 (1988).

[8] S. Hormeño and J. R. Arias-Gonzalez, *Biol. Cell* **98**, 679 (2006).

[9] C. Gosse and V. Croquette, *Biophys. J.* **82**, 3314 (2002).

[10] J. L. Cardy, *J. Phys. A: Math. Gen.* **16**, 3617 (1983).

[11] J. L. Cardy and S. Redner, *J. Phys. A: Math. Gen.* **17**, L933 (1984).

[12] J. L. Cardy, *Nucl. Phys. B* **240**, 514 (1984).

[13] A. J. Guttmann and G. M. Torrie, *J. Phys. A: Math. Gen.* **17**, 3539 (1984).

[14] M. Slutsky, R. Zandi, Y. Kantor and M. Kardar, *Phys. Rev. Lett.* **94**, 198303 (2005).

[15] P.-G. de Gennes, *Scaling Concepts in Polymer Physics* (Cornell University Press, Ithaca, 1979).

[16] M. Doi, *Introduction to Polymer Physics* (Clarendon Press, Oxford, 1996).

[17] P. J. Flory, *Statistical Mechanics of Chain Molecules* (Interscience Publishers, New York, 1969).

[18] P. Pincus, *Macromolecules* **9**, 386 (1976).

[19] S. B. Smith, L. Finzi and C. Bustamante, *Science* **258**, 1122 (1992).

[20] J. F. Marko and E. D. Siggia, *Macromolecules* **28**, 8759 (1995).

[21] B. D. Hughes, *Random Walks and Random Environments*, Vol. 1 (Clarendon Press, Oxford, 1995).

[22] J. Rudnick and G. Gaspari, *Elements of the Random Walk* (Cambridge University Press, 2004).

[23] B. Li, N. Madras and A. D. Sokal, *J. Stat. Phys.* **80**, 661 (1995).

[24] T. Prellberg, *J. Phys. A: Math. Gen.* **34**, L599 (2001).

[25] H.-P. Hsu and P. Grassberger, *J. Chem. Phys.* **120**, 2034 (2004).

[26] A. R. Conway and A. J. Guttmann, *Phys. Rev. Lett.* **77**, 5284 (1996).

[27] E. J. Janse van Rensburg and A. Rechnitzer, *J. Phys. A: Math. Gen.* **41**, 105002 (2008).

[28] N. Clisby, R. Liang, and G. Slade, *J. Phys. A: Math. Theor.* **40**, 10973 (2007).

[29] P. Grassberger, P. Sutter and L. Schäfer, *J. Phys. A: Math. Gen.* **30**, 7039 (1997).

[30] S. Caracciolo, M. S. Causo and A. Pelissetto, *Phys. Rev. E* **57**, R1215 (1998).

[31] B. Nienhuis, *Phys. Rev. Lett.* **49**, 1062 (1982).

[32] A. D. Sokal, in *Monte Carlo and Molecular Dynamics Simulations in Polymer Science*, ed. K. Binder (Oxford University Press, New York, 1995) pp. 47–124.

[33] N. Madras and G. Slade, *The Self-Avoiding Walk* (Birkhäuser, Boston-Basel-Berlin, 1996).

[34] K. Suzuki, *Bull. Chem. Soc. Jpn.* **41**, 538 (1968).

[35] Z. Alexandrowicz, *J. Chem. Phys.* **51**, 561 (1969).

[36] T. H. Cormen, C. E. Leiserson, R. L. Rivest and C. Stein, *Introduction to Algorithms*, 2nd edn. (MIT Press, Cambridge, 2001).

[37] M. Lal, *Molec. Phys.* **17**, 57 (1969).

[38] N. Madras and A. D. Sokal, *J. Stat. Phys.* **50**, 109 (1988).

[39] S. Chandrasekhar, *Rev. Mod. Phys.* **15**, 1 (1943).

[40] M. Abramowitz and I. A. Stegun, *Handbook of Mathematical Functions* (Dover, New York, 1964).

[41] S. G. Whittington, *J. Chem. Phys.* **63**, 779 (1975).

[42] M. N. Barber, A. J. Guttmann, K. M. Middlemiss, G. M. Torrie and S. G. Whittington, *J. Phys. A: Math. Gen.* **11**, 1833 (1978).

[43] J. S. Reeve and A. J. Guttmann, *Phys. Rev. Lett.* **45**, 1581 (1980).

[44] H. Meirovitch and S. Livne, *J. Chem. Phys.* **88**, 4507 (1988).

[45] K. De'Bell, T. Lookman and S. G. Whittington, *Phys. Rev. A* **41**, 682 (1990).

[46] R. Hegger and P. Grassberger, *J. Phys. A: Math. Gen.* **27**, 4069 (1994).

[47] H. W. Diehl and M. Shpot, *Nucl. Phys. B* **528**, 595 (1998).

[48] P. Grassberger, *J. Phys. A: Math. Gen.* **38**, 323 (2005).

[49] M. Lax, *J. Chem. Phys.* **60**, 2245 (1974).

[50] B. Widom, *J. Chem. Phys.* **43**, 3898 (1965).

[51] J. J. Binney, N. J. Dowrick, A. J. Fisher and M. E. J. Newman, *The Theory of Critical Phenomena: An Introduction to the Renormalization Group* (Clarendon Press, Oxford, 1992).

[52] M. Kardar, *Statistical Physics of Fields* (Cambridge University Press, 2007).

[53] W. D. Mccomb, *Renormalization Methods: A Guide for Beginners* (Clarendon Press, Oxford, 2004).

[54] L. Schäfer, *Excluded Volume Effects in Polymer Solutions as Explained by the Renormalization Group* (Springer, Berlin, 1999).

[55] R. J. Rubin, *J. Math. Phys.* **8**, 576 (1967).

[56] G. H. Weiss, *J. Math. Phys.* **22**, 562 (1981).

[57] D. Considine and S. Redner, *J. Phys. A: Math. Gen.* **22**, 1621 (1989).

[58] N. Martzel and C. Aslangul, *J. Phys. A: Math. Gen.* **34**, 391 (2001).

[59] G. Pólya, *Math. Ann.* **84**, 149 (1921).

[60] P. Grassberger, *Phys. Lett. A* **89**, 381 (1982).

[61] H. Meirovitch, *J. Chem. Phys.* **79**, 502 (1983).

[62] H. A. Lim and H. Meirovitch, *Phys. Rev. A* **39**, 4176 (1989).

[63] D. E. Burnette and H. A. Lim, *J. Phys. A: Math. Gen.* **22**, 3059 (1989).

[64] S. Redner and V. Privman, *J. Phys. A: Math. Gen.* **20**, L857 (1987).

[65] E. Eisenberg and A. Baram, *J. Phys. A: Math. Gen.* **36**, L121 (2003).

[66] I. Peschel, L. Turban and F. Iglói, *J. Phys. A: Math. Gen.* **24**, 1229 (1991).

[67] H. S. Carslaw and J. C. Jaeger, *Conduction of Heat in Solids* (Clarendon Press, Oxford, 1959).

[68] C. Vanderzande, *J. Phys. A: Math. Gen.* **23**, 563 (1990).

[69] S. Caracciolo, G. Ferraro and A. Pelissetto, *J. Phys. A: Math. Gen.* **24**, 3625 (1991).

[70] P. Grassberger, *J. Phys. A: Math. Gen.* **26**, 2769 (1993).

[71] S. Caracciolo, M. S. Causo and A. Pelissetto, *J. Phys. A: Math. Gen.* **30**, 4939 (1997).

[72] E. Ott, *Appendix: Hausdorff Dimension*, in *Chaos in Dynamical Systems*, (Cambridge University Press, 1993), pp. 100–103.

[73] D. S. Bulgarevich, K. Mitsui and H. Arakawa, *J. Phys. Conf. Ser.* **61**, 170 (2007).

[74] K. L. Chung, *Markov Chains with Stationary Transition Probabilities*, 2nd edn. (Springer-Verlag, New York, 1967).

[75] S. Caracciolo, M. S. Causo, G. Ferraro, M. Papinutto and A. Pelissetto, *J. Stat. Phys.* **100**, 1111 (2000).

[76] M. S. Causo, *J. Stat. Phys.* **108**, 247 (2002).

[77] M. B. Priestley, *Spectral Analysis and Time Series* (Academic Press, London, 1981).

[78] U. Wolff, *Comput. Phys. Comm.* **156**, 143 (2004).

תקציר

אנו חוקרים מודל סריג של פולימר הצמוד בקצה אחד לגשוש (probe) בלתי-חדיר, בעל גאומטריה מעגלית או פרבולית. תצורה זו דומה לזו המשמשת בניסויים על מולקולות בודדות. נחקרים שלושה מאפיינים עיקריים של הפולימר: ההיפרדות של נקודת הקצה של הפולימר מקצה הגשוש, התגובה לכוח המופעל על הפולימר ומספר המצבים הזמינים לפולימר. המידע מופק ע"י ביצוע סימולציית מונטה קרלו על מודלי סריג בשניים ובשלושה מימדים.

מאפייני הפולימר תלויים ביחס שבין גודלו לבין האורך האופייני של הגשוש. על מנת לתאר את המאפיינים באמצעות פונקציה של יחס זה אנו משתמשים בשיקולי כיול (scaling). תוצאות אנליטיות ניתנות לגבי המאפיינים הצפויים בגבול של פולימרים קצרים מאוד או ארוכים מאוד מהאורך האופייני של הגשוש.

תוצאות הסימולציות עבור שתי הגאומטריות של הגשוש תואמות ברובן לאלו הצפויות באופן תיאורטי בגבולות של פולימרים קצרים וארוכים, ומראות מעבר (crossover) מונוטוני בין שני גבולות אלו. לעומת זאת, התגובה (המנורמלת) לכוח רוחבי (lateral) מגיעה למקסימום ברור כאשר גודל הפולימר הינו מאותו סדר גודל של האורך האופייני של הגשוש. המקסימום הזה ברור במיוחד עבור גאומטרייה מעגלית של הגשוש. בנוסף, מספר המצבים הזמינים לפולימר ליד גשוש פרבולי מראה התנהגות לא צפויה כאשר הפולימר ארוך ביחס לאורך האופייני של הגשוש. אנו מנסים להסביר התנהגות זו באמצעות שני חסמים גאומטריים המאפיינים את הגשוש הפרבולי.

תוצאות העבודה מצביעות על כך שלגשוש תיתכן השפעה ניכרת על הפולימר הצמוד לו כאשר הכוחות המופעלים הם קטנים, ושיש להתחשב בגורם זה בניתוח התיאורטי של תוצאות ניסויים.

TEL AVIV UNIVERSITY
RAYMOND AND BEVERLY SACKLER
FACULTY OF EXACT SCIENCES
SCHOOL OF PHYSICS & ASTRONOMY

אוניברסיטת תל-אביב
הפקולטה למדעים מדויקים
ע״ש ריימונד ובברלי סאקלר
בית הספר לפיסיקה ואסטרונומיה

מכניקה סטטיסטית של פולימרים בקרבת גשושים דוחים

חיבור זה הוגש כחלק מהדרישות לקבלת התואר
"מוסמך אוניברסיטה" – M.Sc. באוניברסיטת תל-אביב
בית הספר לפיסיקה ואסטרונומיה

על-ידי

רועי בוביס

העבודה הוכנה בהדרכתו של פרופסור יעקב קנטור

אפריל 2009